CFD EXPERIMENTS ON A LOW CRESTED SLOPING TOP CAISSON BREAKWATER. PART 1. NATURE OF LOADINGS AND GLOBAL STABILITY

Mariano Buccino[1], Mohammad Daliri[1], Fabio Dentale[2], Angela Di Leo[2], Mario Calabrese[1]

1. *Dept. of Civil, Architectural and Environmental Engineering, University of Napoli "Federico II". Via Claudio 21, 80125, Napoli, Italy.*
2. *Maritime Engineering Division, University of Salerno. Via Giovanni Paolo II, Fisciano (SA)*

Keywords: *Numerical modeling, Computational Fluid Dynamics, Sloping top breakwater, wave force, wave impact.*

ABSTRACT

Random wave CFD experiments have been carried out to study the loading process on a sloping top caisson breakwater subject to significant overtopping. Numerical results suggest that since wave force under crest is reduced by the overpassing, wave pressures under trough become comparatively larger, leading the structure to fail seaward even in absence of violent impact events; this finding is consistent with what observed by Oumeraci (1994) in reviewing the failures of a number of vertical face breakwaters during the first half of 20th century. Present findings also show that wave pressures under trough may be significantly underestimated by the design formulae currently available. To face this issue, a set of simple alternative equations are proposed, based on the maximum momentum flux concept, originally introduced by Hughes (2004).
A second part of the research work is dedicated to the occurrence of intense impulsive loadings at rear of the breakwater, caused by the huge inertia of the overtopping jet. The analysis of this interesting phenomenon is though presented in a separate paper.

1. INTRODUCTION

Monolithic breakwaters have been employed for the protection of harbor areas since times before the ancient Roman Empire. The most common type, generally referred to as "vertical face" breakwater or "vertically composite" breakwater, consists of an upright wall rested on a foundation mound.
As well documented by Oumeraci (1994), in first half of the 20th century such kind of structures suffered from catastrophic failures, which led to their almost complete abandoning. Many of those breakdowns were caused by tremendous wave forces, associated with wave breaking and featured by an impulsive nature.
However, nearly 50 years later, the need for structures at large water depths with a relatively low cost, reignited the interest about vertical face breakwaters, giving rise to an intense research work; the latter culminated in the EU funded project PROVERBS (PRObabilistic design tools for VERtical BreakwaterS), which gathered together the most important European research groups (Oumeraci et al., 1999).
In those years, the effort of scientists was addressed at either improving the knowledge about the wave-structure interaction or suggesting solutions to reduce the intensity of hydrodynamic loadings exerted on the walls.

Many milestone papers were dedicated at describing the mechanics of wave breaking and the related impulsive loadings (Cooker and Peregrine, 1990 Kirkgoz 1991, Hattori and Arami 1992, Oumeraci et al.

1993); the authors recognized that under heavy plunging breakers, air tends to be trapped between wave and structure, so cushioning the impact of most of water mass (Peregrine, 2003). However, the maximum pressure was observed prior the air trapping, and was caused by the direct collision between the plunging water jet and the wall ("hammer shock", see also Lundgren, 1969).

Following an interesting alternative approach, some research focused instead on the "loading case predictability", that consists in individuating the hydraulic conditions under which impulsive or quasi- static forces tend to take place (Oumeraci et al., 1999; Calabrese and Buccino, 2001; Calabrese et al., 2001).

As for the strategies to reduce the intensity of wave actions, the solutions proposed in literature basically include lowering of the breakwater crest, so to allow a significant wave overtopping under the design storm, and changing of the outer profile from perfectly vertical to inclined or curvilinear.

Yet, significant uncertainties still remain on the effectiveness of those suggestions, essentially due to the stalling of the research work in the new millennium.

Thus, despite commonly accepted by engineers, the beneficial role of wave overtopping is not completely demonstrated.

Goda (1995) reasoned that, historically, the low crest of Japanese vertical-face breakwaters(traditionally 0.6 times the design wave height) prevented structures from being damaged by violent impact loadings. Conversely, the aforementioned case histories presented by Oumeraci (1994), reported a number of examples in which the walls failed just after experiencing severe overtopping; it should be noticed, then, that failures occurred often seaward.

In actuality, at current state of knowledge, the prediction of the design wave loadings at low crested monolithic breakwaters is affected by two sources of uncertainty, and namely:

1. since wave overtopping reduces the horizontal force under wave crest, loadings under wave trough become comparatively more important; however, the reliability of the existing design methods for such a wave phase has been little investigated. For conventional non overtopped vertical face breakwaters, a laboratory study by McConnell et al.(1999) showed that significant underpredictions could occur, but this result has been not analyzed further;
2. engineers are used to accounting for wave overtopping effects by simply truncating the wave pressure distributions valid for non overtopped breakwaters; this means loadings generated by the overtopping process onto the inner face of the structure are considered negligible, but this assumption is far from being scientifically ascertained.

Regarding the previous point 2, Walkden et al. (2001) warned that massive overtopping may cause intense impulsive loadings at rear of the structure, due to the huge inertia of the overtopping jet. The authors referred to this phenomenon as "plume impact" and hypothesized it to be significantly affected by the air trapped between the jet and the wall, since a non negligible amount of momentum might be transferred from the air cushion to the water column. Unfortunately, the research of Walkden et al.(2001) was based on small scale physical model tests conducted on three individual waves only and, accordingly, the features of the "plume impact" could not be appropriately investigated.

Information on wave loadings at inclined or curvilinear walls, generally come from regular wave laboratory studies; the main results of those works consist in prediction formulae (e.g. Tanimoto and Kimura, 1985; Takahashi et al, 1994b), which slightly modify the traditional design tools valid for vertical structures. These "new" predictive equations need to be further verified, especially

under random wave
conditions; additionally, more details on other aspects of the wave-structure interaction (such as shape of wave profiles at walls, loading case prediction, etc.) would be desirable, similarly to what accomplished for vertical face breakwaters.

This study aims to give a contribution at filling the research gaps previously highlighted, analyzing the loadings exerted by random waves on a “sloping top” caisson breakwater subject to significant overtopping.

“Sloping top” caisson breakwaters (the first built in Napoli, Italy in 1906) possess a sloping roof that convert part of the wave action into a downward directed force that aids the stability under crest. Such kind of structure was used by Walkden et al. (2001) when investigating the “plume impact”, while Takahashi et al (1994b) developed a design formula to predict wave pressures under crest, which modifies the well-known equation of Goda (1986) for vertical face breakwaters.

The analysis has been carried out via numerical experiments conducted in a Computational Fluid Dynamics (CFD) wave flume, based on the commercial code FLOW-3D (Flow Science Inc., 2009). The CFD technique, which solves numerically the Navier-Stokes equations, is recently growing popular in the field of coastal and ocean engineering (e.g. Jun and Meng, 2011 Kamath, 2015; Antonini et al., 2016, 2017; Miquel et al., 2018) and has proved rather efficient in describing the loading process at monolithic coastal structures, even under breaking waves (Vicinanza et al., 2015; Buccino et al., 2016). In case of relatively little-researched topics, like are partly those treated here, the use of CFD allows providing very detailed information on the phenomena under study, since a great deal of probes can be employed at once; this feature is of course essential for the comprehension of physical processes and planning of future research works. Finally, a breakwater at full scale can be simulated, so reducing scale effects (Cuomo et al., 2010), and the experiments can be repeated with and without the presence of air (see Gaeta and Lamberti, 2015)

The present research is divided into two parts. After discussing and validating the numerical model (Sections 2 and 3), this article deals with wave shapes at the outer face of a sloping top breakwater, loading case predictability and reliability of the available design tools in predicting wave force under both the crest and the trough phases.

The second part of the research (Buccino et al, 2019) is instead expressly dedicated to the analysis of “plume impact”.

2. GOVERNING EQUATIONS AND TURBULENCE CLOSURE

It is assumed the physical processes here investigated to be governed by the Reynolds Averaged Navier-Stokes Equations (RANS) for incompressible fluids. In a 2D reference where the x axis is perpendicular to the coast (onshore directed) and the z axis is vertical (upward directed), the continuity equation reads:

$$\frac{\partial u}{\partial x} + \frac{\partial w}{\partial z} = 0 \tag{1}$$

where u and w are the turbulence averaged velocity components, along x and z respectively. The momentum equations are:

$$\frac{\partial u}{\partial t} + u\frac{\partial u}{\partial x} + w\frac{\partial w}{\partial z} + \frac{1}{\rho}\frac{\partial p}{\partial x_i} - 2\frac{\partial}{dx}\left[(\nu + \nu_T)\frac{\partial u}{\partial x}\right] - \frac{\partial}{dz}\left[(\nu + \nu_T)\left(\frac{\partial u}{\partial z} + \frac{\partial w}{\partial x}\right)\right] = 0 \tag{2}$$

$$\frac{\partial w}{\partial t} + u\frac{\partial w}{\partial x} + w\frac{\partial w}{\partial z} + \frac{1}{\rho}\frac{\partial p}{\partial z} + g - \frac{\partial}{dx}\left[(\nu + \nu_T)\left(\frac{\partial u}{\partial z} + \frac{\partial w}{\partial x}\right)\right] - 2\frac{\partial}{dz}\left[(\nu + \nu_T)\frac{\partial w}{\partial z}\right] = 0 \qquad (3)$$

where ρ is the fluid density, g is gravity, p is the turbulence averaged pressure and v is the kinematic
viscosity. The eddy viscosity v_T is expressed as:

$$\nu_T = c_\mu f_\mu \cdot \frac{k^2}{\varepsilon} \qquad (4)$$

where k is the turbulent kinetic energy, ε is the dissipation rate of k, cμ is an empirical constant and fμ is a damping factor; the latter reduces exponentially with the turbulence Reynolds number RT= k 2/vε.

To determine k and ε, two additional transport equations must be solved:

$$\frac{\partial k}{\partial t} + u\frac{\partial k}{\partial x} + w\frac{\partial k}{\partial z} - \frac{\partial}{dx}\left[\frac{(\nu + \nu_T)}{\sigma_k}\frac{\partial k}{\partial x}\right] - \frac{\partial}{dz}\left[\frac{(\nu + \nu_T)}{\sigma_k}\frac{\partial k}{\partial z}\right] + \varepsilon - P = 0 \qquad (5)$$

$$\frac{\partial \varepsilon}{\partial t} + u\frac{\partial \varepsilon}{\partial x} + w\frac{\partial \varepsilon}{\partial z} - \frac{\partial}{dx}\left[\frac{(\nu + \nu_T)}{\sigma_\varepsilon}\frac{\partial \varepsilon}{\partial x}\right] - \frac{\partial}{dz}\left[\frac{(\nu + \nu_T)}{\sigma_\varepsilon}\frac{\partial \varepsilon}{\partial z}\right] + c_2\frac{\varepsilon^2}{k} - c_1\frac{\varepsilon}{k}\nu_T P = 0 \qquad (6)$$

where the shear production, P, is defined as:

$$P = \frac{(\nu + \nu_T)}{\rho}\left\{2\left(\frac{\partial \mathrm{u}}{\partial x}\right)^2 + \left(\frac{\partial \mathrm{u}}{\partial z} + \frac{\partial w}{\partial x}\right)^2 + 2\left(\frac{\partial \mathrm{w}}{\partial z}\right)^2\right\} \qquad (7)$$

Eqs. (5)–(7) represent the widely known standard k-ε turbulence model, where, σk, σε, c1 and c2 are additional constants (Launder and Spalding, 1974).

However, in this study, a ReNormalized Group (RNG) extension of the above model has been used (RNG); here, the parameters cμ, c1, σk and σε still remain constant (cμ=0.085, c1=1.42, σk=σε=1.39), whereas c2 is assumed to vary with P according to the formula (Yakhot et al., 1992):

$$c_2 = 1.68 + \frac{c_\mu \beta^3 (1 - 0.2283\beta)}{1 + 0.012\beta^3} \qquad (8)$$

$$\beta = \frac{k}{\varepsilon}\sqrt{\frac{P}{(\nu + \nu_T)}} \qquad (9)$$

By allowing c_2 to vary with the fluid strain rate, a presumably more general model is obtained that should yield more accurate results for strongly sheared flows (Bradford, 2000). In this respect, it is interesting to remark that comparing numerical CFD simulations to the experiments of Ting and Kirby (1994), Bradford (2000) found out the RNG closure to be more effective than standard k-ε model in simulating the evolution of plunging breakers both prior and just after the onset of breaking. This result is particularly useful for the present research, where waves have been observed to break in wise of plunging breakers at a short distance from the structure. Fluid configurations are defined in terms of a Volume of Fluid (VOF) function F(x,y,z,t) (Hirt and Nicholas, 1981), which represents the volume of fluid that occupies a portion of space of unitary

volume. F satisfies the following transport equation:

$$\frac{\partial F}{\partial t} + u\frac{\partial F}{\partial x} + w\frac{\partial F}{\partial z} = 0 \tag{10}$$

For a single incompressible fluid with a free surface, fluid exists where F=1, while locations where F=0 correspond to void regions, in which a uniform pressure is applied. In case of two incompressible fluids with no free surface, F represents the volume fraction of the fluid#1, whereas the complementary region with volume fraction 1 – F represents fluid #2.

3. NUMERICAL SOLUTION

The equations above described have been finite-difference solved, via the commercially available multi-physics CFD software "FLOW-3D". Developed by Flow Science Inc. (2009), FLOW-3D has been recently employed, with satisfactory results, in a number of wave-structure interaction problems, including both impermeable walls and permeable breakwaters (e.g. Buccino et al., 2016; Vicinanza et al., 2015, Dentale et al., 2014a, 2014b).

The flow region is subdivided into a mesh of fixed rectangular cells, at center of which are located all the variables but velocities, which are situated, instead, at the cell–faces (staggered grid arrangement).
Curved obstacles, wall boundaries, or other geometric features are embedded in the mesh by defining the fractional areas of the cells that are open to flow (FAVOR™ method (Hirt and Sicilian 1985).

The governing equations are discretized as follows:

$$\frac{u_{i+1\,j}^{n+1} - u_{ij}^{n+1}}{\Delta x} + \frac{w_{ij+0.5}^{n+1} - w_{ij}^{n+1}}{\Delta z} = 0 \tag{11}$$

$$\frac{u_{ij}^{n+1} - u_{ij}^{n}}{\Delta t^{n+1}} = -\left(A_{ux} + A_{uy} + A_{uz}\right)_{ij}^{n} - (VIS_x)_{ij}^{n} - \frac{2}{\rho_{ij}^{n} + \rho_{i+1\,j}^{n}}\left(\frac{p_{i+1\,j}^{n+1} - p_{i\,j}^{n+1}}{\Delta x}\right) \tag{12}$$

$$\frac{w_{ij}^{n+1} - w_{ij}^{n}}{\Delta t^{n+1}} = -\left(A_{wx} + A_{wy} + A_{wz}\right)_{ij}^{n} - (VIS_z)_{ij}^{n} - \frac{2}{\rho_{ij}^{n} + \rho_{i\,j+1}^{n}}\left(\frac{p_{i+1\,j}^{n+1} - p_{i\,j}^{n+1}}{\Delta z}\right) \tag{13}$$

where the subscripts indicate the cell coordinates and the superscripts indicate time step. Δx and Δz represent the cell length and height respectively, while Δt is the time step size (see subsection 3.1).

In the momentum equations, both the advective fluxes (Aαβ) and the viscous terms ($\boldsymbol{VISx,z}$) are calculated explicitly, using the old time level n, according to the first order donor cell approximation method. As far as the fluid density (ρ) is concerned, a single value is used in case of one incompressible fluid flow, whereas a weighted average over the VOF function F is employed for two incompressible fluids.

Since in Eqs. (11)- (13) pressures and velocities are coupled implicitly, an iteration solution procedure is needed. To this purpose, the momentum balance is firstly solved using the pressure gradient at the time level n; this gives an intermediate velocity vector, $\overrightarrow{U^*}$, which is linked to the real velocity at the time step n+1 ($\overrightarrow{U^{n+1}}$), by the following relationship:

$$\overrightarrow{U^{n+1}} = \overrightarrow{U^*} + \frac{2 \cdot \Delta t^{n+1}}{\rho_{ij}^n + \rho_{i+1\,j}^n} \nabla p' \tag{14}$$

Where $p' = p^{n+1} - p^n$. By inserting Eq. (1) in Eq. (), a Poisson equation in p' is obtained, which is solved through the Generalized Minimum RESidual method (GMRES; Saad,1996).
After obtaining $\overrightarrow{(U^{n+1})}$, the new free surface configuration is computed with the VOF method while k and ε are computed using analogous discretizations of (5) and (6).

3.1 Stability considerations

Flow-3D uses variable time stepping to maintain the stability and accuracy of the solution. In particular, the n-th time step size, Δt^n, is automatically adjusted to:

$$\Delta t^n = \min(\Delta t_{CON}^n, \Delta t_s) \tag{15}$$

where Δt_s is a user defined sampling rate, which depends on the frequency spectrum of the phenomenon under study, and Δt^n_{CON} is a convergence time step size, that is needed to avoid numerical instabilities. Since the advective fluxes have been computed using a simple first order donor cell, Δt^n_{CON} is required to meet the following criterion:

$$\Delta t_{CON}^n = \min(0.5 \cdot \Delta t_{CFL}, 0.5 \frac{\Delta x}{\sqrt{\Delta z \Delta az}}) \tag{16}$$

where Δt_{CFL} is the time step to satisfy the Courant–Friedrichs–Lewy (CFL) stability criterion and the second quantity at the right-hand side of Eq. () ensures surface waves cannot propagate more than one cell in one time step (*az* indicates vertical acceleration).

3.2 Validation study

To validate the numerical model above described with respect to the interaction between waves and sloping walls (with a particular focus on the loading process and wave shape at the structure), a comparison with the 2D physical model tests carried out by Buccino et al. (2015) is here presented.

The lab experiments were conducted on a small scale model of Seawave Slotcone Generator (SSG), a Wave Energy Converter based on the overtopping principle (Vicinanza et al., 2012). The SSG has been placed on the top of a steep multi-linear slope, seaward of which the water depth (d) has been kept constant (Figure 1a). Regular waves with different height and period have been generated and the

hydrodynamic pressures have been acquired via four resistive transducers (Figure 1b), sampled at 1kHz.

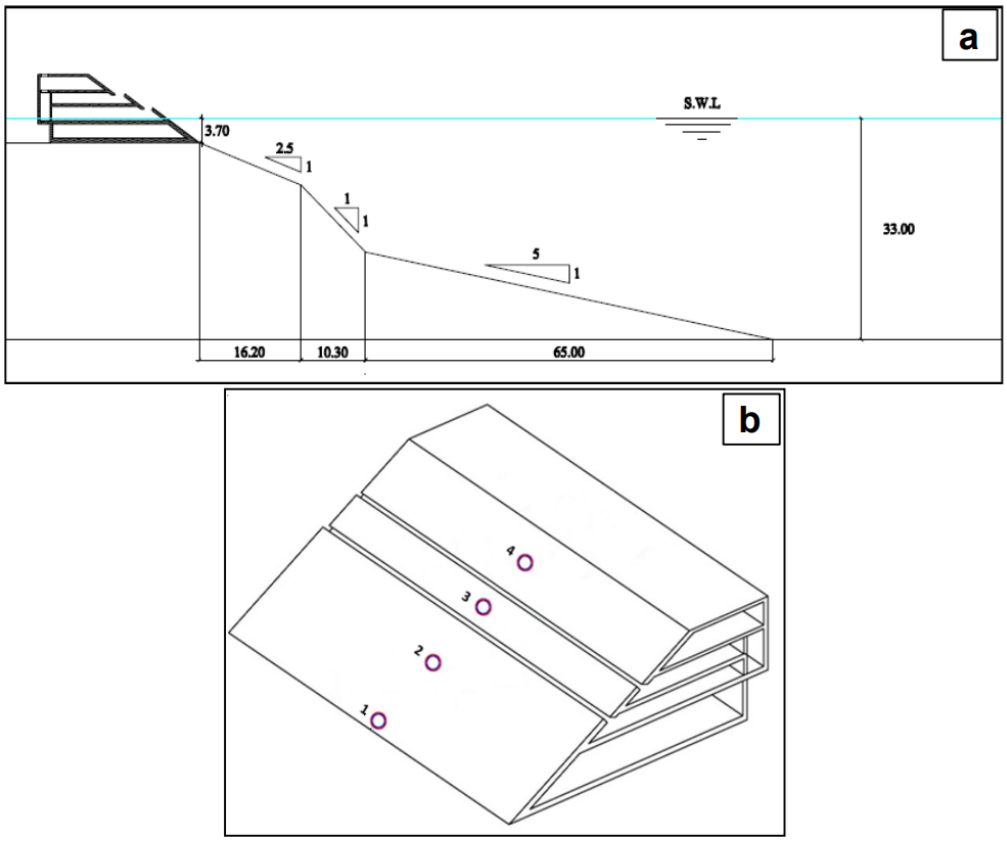

Figure 1. *Sketch of the Buccino et al.(2016) experiments. a: profile of SSG and foreshore (dimensions in m at prototype scale); b: view of the structure.*

The numerical flume (Figure 2) has been set-up at full scale and reproduces un-distortedly both the SSG and the foreshore.

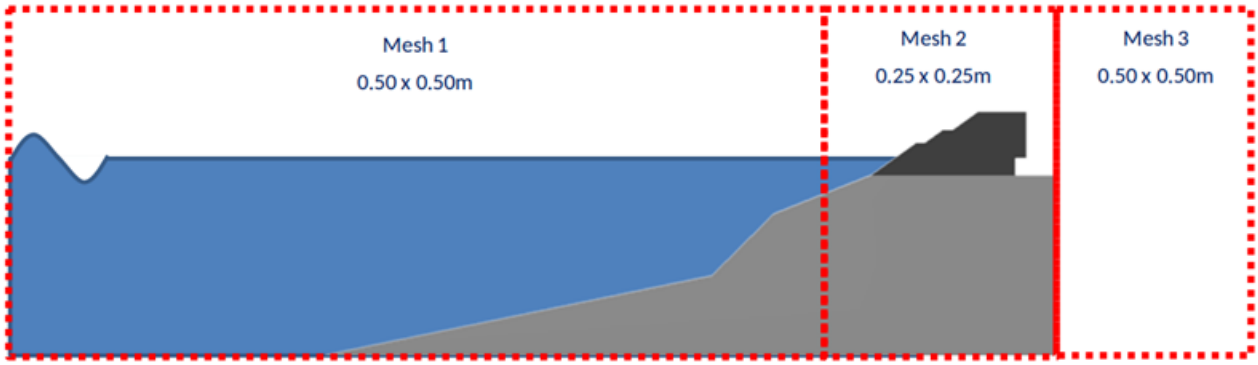

Figure 2. *Sketch of the numerical flume.*

According to the sensitivity analysis described in Buccino et al. (2016), the computational domain (400m in the x direction and 60m in the z direction) has been divided into three zones: the meshes 1

and 3 include 62,400 and 14,400 cells respectively, the size of which is 50 x 50 cm; the local mesh that surrounds the WEC (mesh 2) consists instead of 38400 cells 0.25x0.25m.

For the aims of the present work, two experiments have been selected, whose wave parameters, calculated at the flat part of the flumes, are reported in Table 1. Note that numerical experiments have been carried out with a single incompressible fluid.

Given the Urserll number HL2/d3 do not exceed 2.0, numerical regular waves have been generated using the linear wave generator available in FLOW-3D.

Lateral and upper limits of the numerical flume have been treated as “Symmetry boundaries” (S), where the velocity gradient vanishes and the turbulence production is zero. Also, a zero flow area has been here imposed that automatically ensures no advective or diffusive fluxes.

At the bottom, a “wall condition” (W) has been set, implying no-slip, as well as zero velocity gradient.

Since FLOW-3D includes no active absorption system, only the part of the numerical loading signals that is unaffected by re-reflection at the wave generator has been considered for the analysis (see subsection 4.6).

From Table 1 it is seen lab and numerical wave heights to differ by 10% at most, whereas wave periods deviate from each other by few percents only.

Table 1. Wave parameters (at prototype scale) for validation tests. Values calculated at the flat part of the flumes

	CFD		Physical model		REL-Difference [%]		Sampling rate [s]	
TESTCODE	H [m]	T [s]	H [m]	T [s]	H	T	**CFD**	**Phys**
V-A	2.61	8.01	2.37	8.12	10	1	0.4	0.008
V-B	7.71	8.00	7.62	8.12	1	2	0.008	0.008

For test V-A a simple quasi-standing wave with no overtopping was observed (Figure 3).

As shown in Figure 4 the numerical model satisfactorily reproduces duration and shape of loadings, besides their magnitude. In particular, panels b and c suggest the non linearity of pressure time series is well captured, whereas panel d ensures no overtopping has taken place, since the pressure signals have a zero amplitude.

Figure 5 compares the wave profiles at the wall during test V-B, which corresponds to a heavy plunging breaker. The numerical model properly reproduces:

- the hammer shock, which occurs approximately at the SSG toe (first panel from the top);
- the secondary splash-up (Buccino et al., 2015), where the water mass hits again the structure onto the higher plate (second panel);
- the overtopping phase (third and fourth panel)

The impacts generated by the hammer shock and secondary splash-up produce impulsive pressure events at the transducers 1 and 3, which are realistically simulated in the numerical flume, as shown in Figure 6.

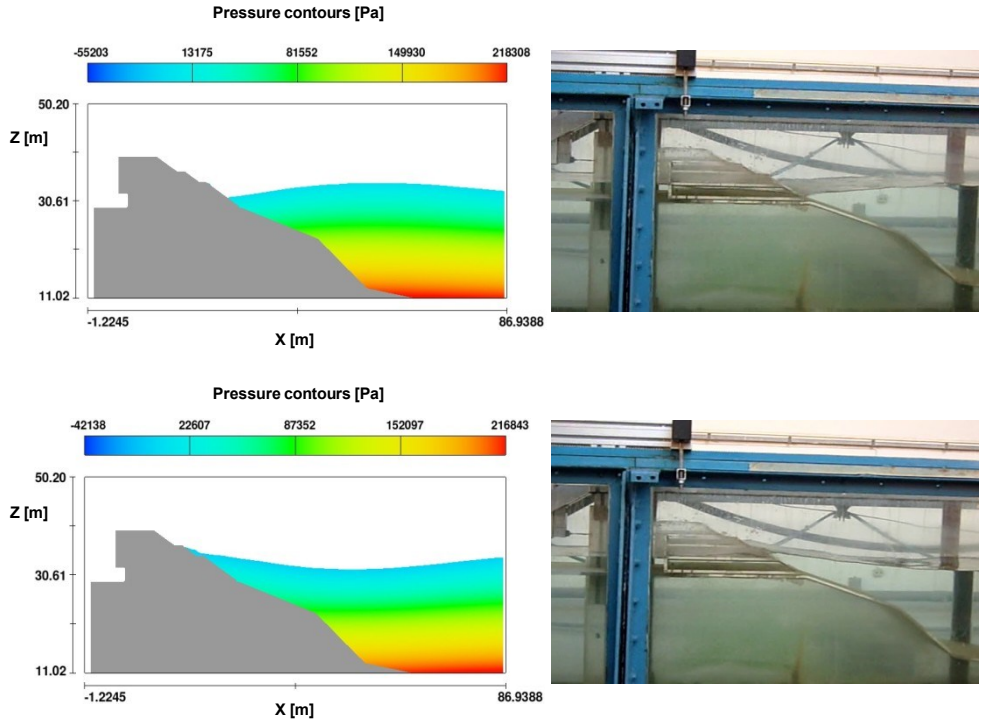

Figure 3. *Wave profile for test V-A*

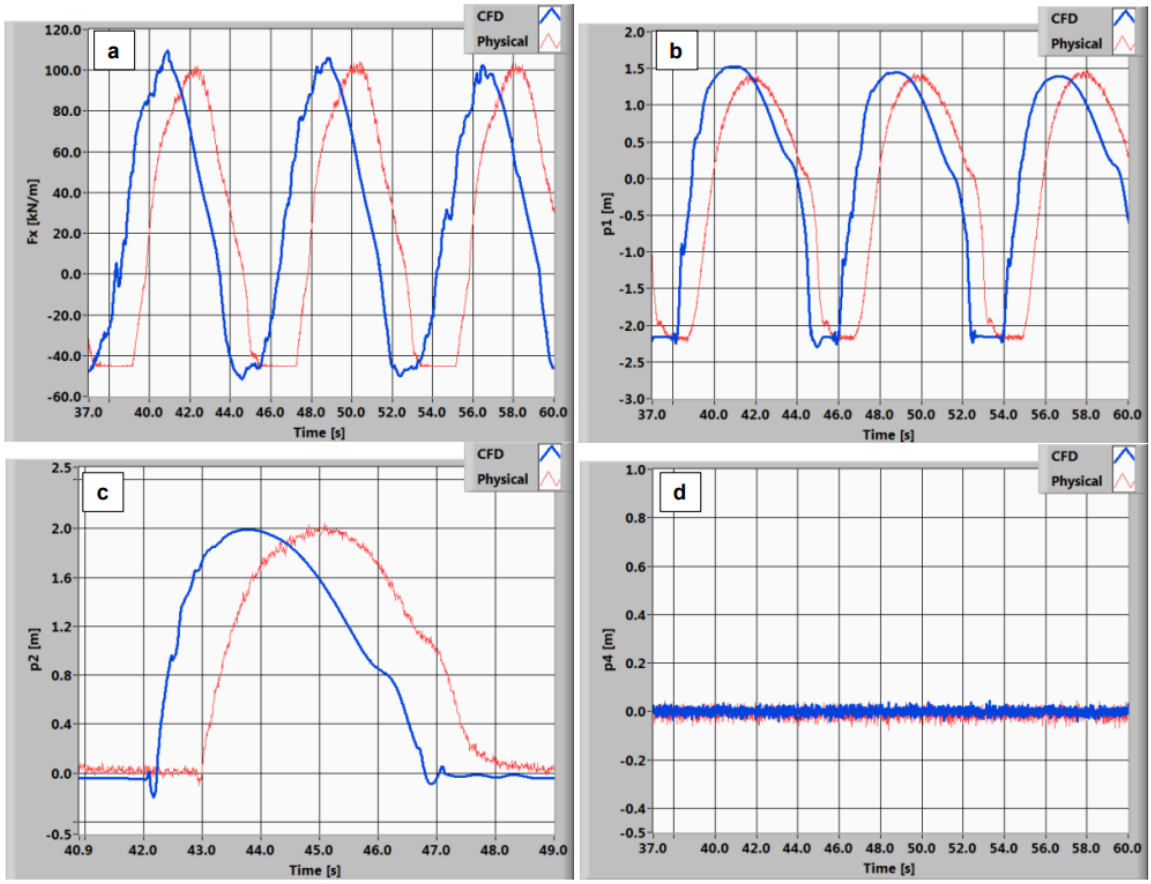

Figure 4. *Force and pressure signals for test V-A. Panel a: horizontal force in N/m; panel b: pressure transducer #1; panel c: pressure transd. #2; panel d: pressure transd. #4.*

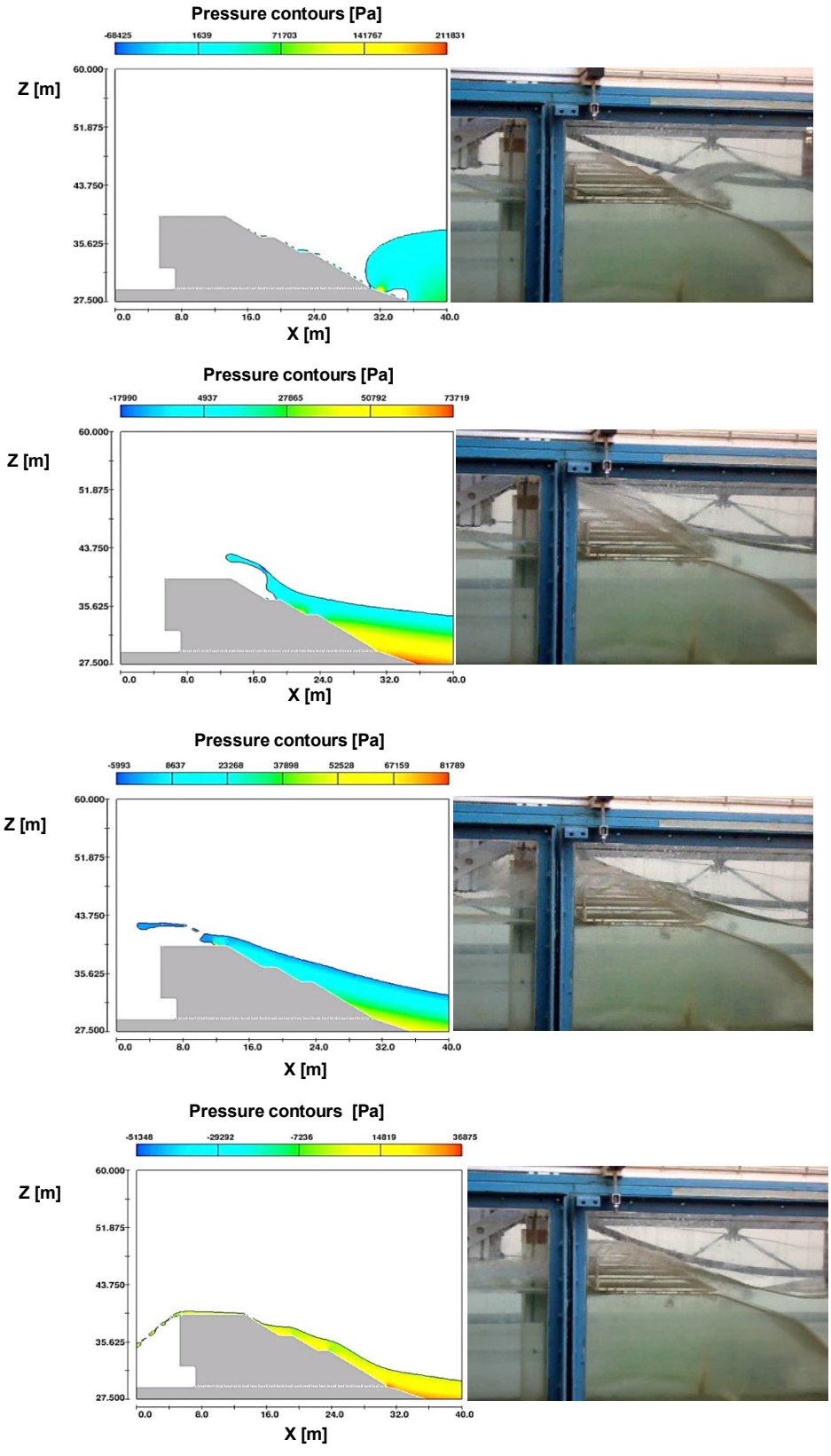

Figure 5. Wave Profile for test V-B

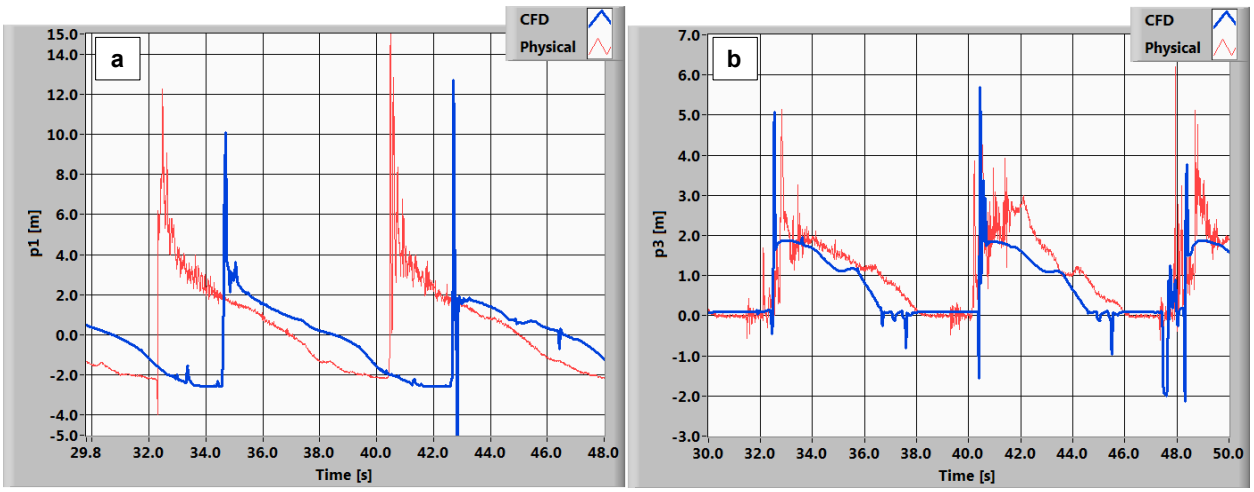

Figure 6. *Pressure signals (in m) for test V-B. Panel a: transducer 1; panel b:transducer 2.*

4. STUDY OF A SLOPING TOP BREAKWATER

To investigate the structural response of sloping top breakwaters , the “full-scale” numerical wave flume pictured in Figure 7 has been employed.

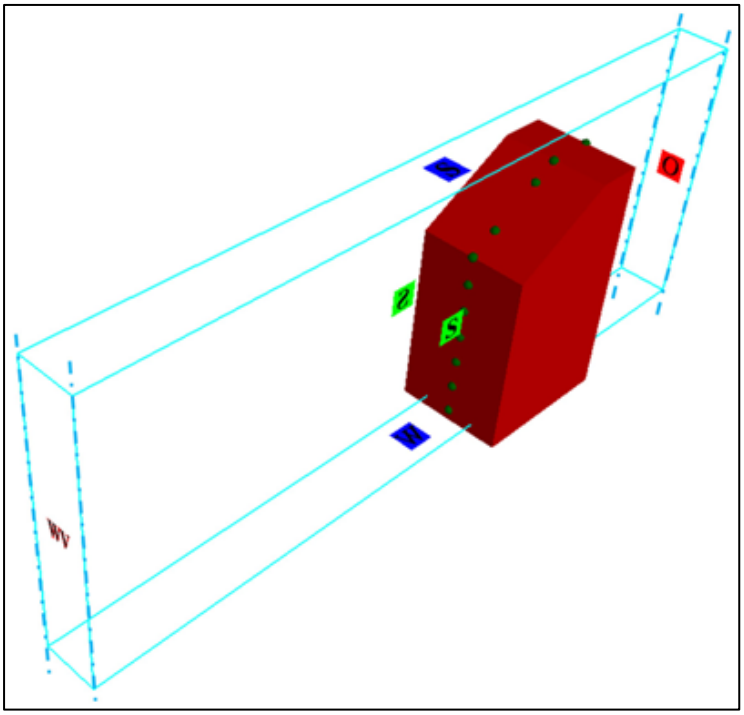

Figure 7. Axonometric view of the numerical flume

The structure is located 300m far from the wavemaker (WV); at the rear of the wall, the channel continues by 200 m, up to an “outflow” boundary (O), which let the waves to flow out without any reflections.

Lateral walls, flume upper and limit bottom have been subjected to the same boundary conditions as those described in Section 3.2.

4.1. Structure details

The structure tested (Figure 8) has a total height of 21.42m and the sloping part is inclined to the horizontal by θ=30°. The height of the sloping top, S, is 5.39m, whilst the upright section, V, measures16.03m. The sea floor is constant, with a still water depth d = 18.9m.
Altogether, the structure is rather similar to that used by Walkden et.al (2001), who tested a caisson
with the same S to V ratio (0.34) and θ= 35°. On the other hand, Takahashi et.al (1994b) employed °
steeper tops (θ = 45° and 56°) and S/V ranging from 0.26 to 0.92.

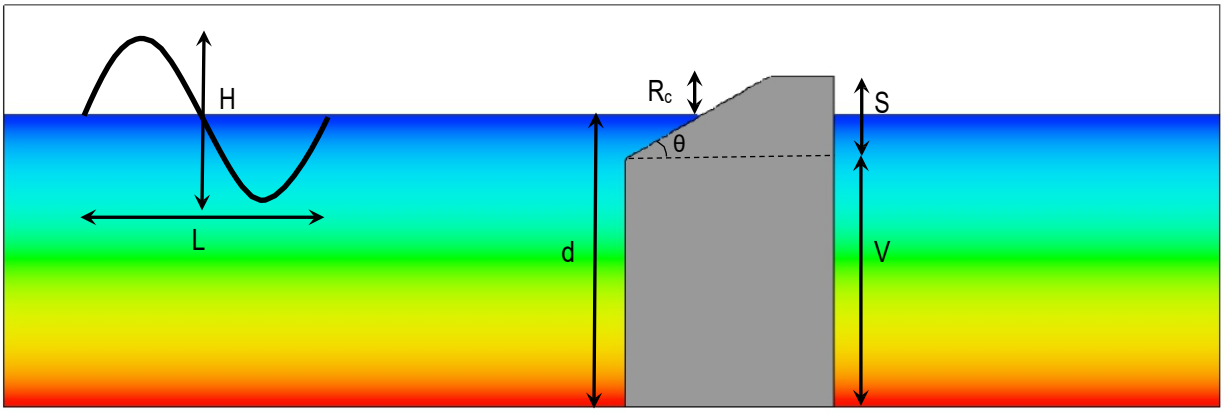

Figure 8. Sketch of the structure tested

A leading feature of the breakwater here considered is that the lower tip of the sloping face is located 2.87m underwater, whereas in Walkden et al. (2001) it was just at the mean water level. As shown later in the paper, this characteristic, which might be generated by a rise of the mean sea level under the design storm, could of course affect the statics of the structure; this because while enhancing the stability under wave crest, an upward directed component of the wave force tends to take place at the sloping top under the trough phase.

It is also noteworthy that four structures out the six considered in the Takahashi et al. (1994b) study had a partially submerged sloping profile.

4.2 Grid selection

In order to select the most appropriate grid dimensions, a sensitivity study has been conducted. Three rectangular grids with different cell size have been tested and namely:

- 0.5m (horizontal) x 1m (vertical);
- 0.25m x 0.5m;

- 0.125m x 0.25m.

For each mesh, the structure has been subjected to a train of 30 regular waves and the signal of the horizontal force exerted onto the front face has been acquired. Wave generation has been carried out via the cnoidal wave generation tool available in FLOW-3D.

The generated waves (H=4.4m and T=8s) have been preliminarily checked to reach the structure without breaking, in order the sensitivity analysis were not affected by the inherent randomness of loadings induced by breaking waves (Buccino et al., 2015; Peregrine 2003).

It is also worth noticing that for each grid, FLOW-3D uses variable time stepping to maintain the stability and accuracy of solution (see Subsection 3.1)

As shown in Figure 9, the widest grid tends to create deep troughs that are not observed with the finer ones; on the other hand, the results for 0.25m x 0.5m and 0.125m x 0.25m are very similar to each other.

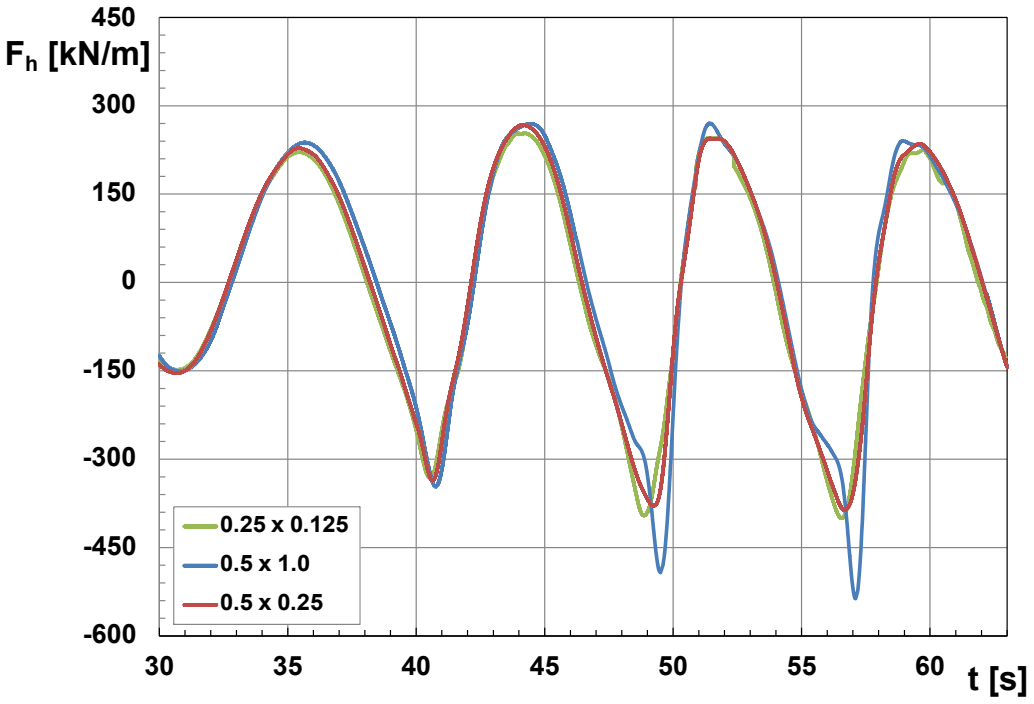

Figure 9. Force time series for different grid size

To measure the degree of convergence, two indicators have been introduced and namely:

a) The "*relative error*" from the wider to the finer grid, defined as:

$$Rs = \frac{StDev[F_{wide} - F_{fine}]}{\max(F_{fine})} \tag{17}$$

where F represents the force signal and the subscripts "wide" and "fine" refer to the wider and the finer grid used. The symbol "Stdev" indicates standard deviation.

b) The square correlation between the force signals:

$$R^2 = \frac{E[F_{wide} \cdot F_{fine}]}{StDev\,(F_{wide}).\ StDev\,(F_{wide})} \quad (18)$$

in which E indicates statistical expectation.

Results of the analysis are summarized in Table 2, which confirms the substantial coherence between the grids 0.5m x 0.25m and 0.25m x 0.125m (R2 exceeds 99%). Accordingly, the former has been selected for the final experiments.

Table 2. Values of convergence indicators

Wide	Fine	R_s	R^2
0.5m x1m	0.5m x 0.25m	0.39	0.961
0.5m x 0.25m	0.25m x 0.125m	0.045	0.995

4.3. Waves and hydraulic variables

Eleven sea states have been generated, lasting approximately 30 waves. Each sea state was driven by a very narrow banded spectrum; accordingly, the incoming waves had almost the same period, whereas their height could vary. Narrow banded wave series have been first generated numerically, through a specific code written in LABVIEW; then, the power spectrum has been calculated and used as input for wave generation in FLOW-3D.

Table 3 reports the main wave statistics, whilst Table 4 shows some relevant non-dimensional variables, as well as sampling rate (ΔtS.). Note that the Ursell number at the fifth column is calculated as:

$$Ur = \frac{H_{m0} L_p^2}{d^3} \quad (19)$$

in which Hm0 is the spectral significant wave height and Lp is the local wavelength, obtained by the linear dispersion relationship using the peak period Tp

Table3. Main statistics of generated sea states

TESTCODE	H_{m0} (m)	T_p (s)	H_{mean} (m)	T_{mean} (s)	H_{max} (m)	T_{max} (s)
1A	4.9	6.32	4.07	6.38	5.56	6.37
1B	3.65	6.41	3.37	6.45	3.84	6.11
1C	3.04	6.44	2.53	6.59	3.39	6.27
2A	5.58	11.56	4.75	11.87	6.64	11.83
2B	4.70	11.92	3.92	11.87	5.55	12.03
2C	3.47	11.86	2.63	11.7	4.22	12.10
N1	4.41	7.93	4.04	8.08	4.49	7.81
N2	5.24	7.97	4.76	8.08	5.45	7.62
3A	7.078	11.89	5.8	11.77	8.19	12.48
3B	5.06	12.21	4.2	11.85	5.61	12.32
4A	6.21	6.74	5.38	6.85	6.39	6.79

Table4. Non Dimensional variables along with the sampling rate (ΔtS) and the total simulation time

TESTCODE	H_{m0}/L_p	d/L_p	R_c/H_{m0}	H_{m0}/d	U_r	Δt_S (s)	Total simulation time (s)
1A	0.082	0.315	0.514	0.259	2.615	0.008	265
1B	0.059	0.307	0.690	0.193	2.045	0.008	265
1C	0.049	0.305	0.829	0.160	1.731	0.008	265
2A	0.039	0.133	0.452	0.295	16.762	0.015	480
2B	0.032	0.128	0.536	0.248	15.200	0.008	480
2C	0.024	0.129	0.726	0.183	11.087	0.015	480
N1	0.051	0.219	0.571	0.233	4.874	0.008	240
N2	0.060	0.217	0.481	0.277	5.856	0.008	240
3A	0.048	0.128	0.356	0.374	22.753	0.008	480
3B	0.033	0.124	0.498	0.267	17.329	0.008	480
4A	0.093	0.282	0.406	0.328	4.123	0.004	265

The range of wave steepness (H/L= 0.024-0.093) is almost identical to that tested by Takahashi et.al (0.023-0.109) and same goes for relative water depth d/L (0.124-0.315 vs. 0.09-0.23).

As far as relative crest freeboard is concerned, the present study focuses on structures subject to significant overtopping (Rc/H = 0.356-0.829), whereas Takahashi et al. extended their analysis to non overtopped breakwaters too (Rc/H = 0.321-3.81).

It is also worth to mention that the three individual waves tested by Walkden et.al (2001) had a 0.17m

height and a 1s period, corresponding to a wave steepness of 0.11 and a relative crest freeboard 0.558. It is finally noteworthy that waves travelled by 2-5 wavelengths before reaching the structure; while this distance ensures them to be properly developed on the flat bottom, it substantially dampens the effects of undesired phenomena of turbulence over-production, as recently shown by Larsen and Fuhrman (2018). In fact, the authors concluded that the short propagation distance allotted prior the onset of breaking limits the turbulence overproduction problem even in the post breaking phase.

4.4 Fluid properties

The experiments from 1A to N2 have been conducted with a single fluid (water), i.e. neglecting any effect of air; on contrary, in the tests 3A, 3B and 4A, the presence of air has been accounted for, using the “two fluid model option” of FLOW-3D . Accordingly, the properties of water and air (density, viscosity) have been assigned separately and the governing equations have been solved for all fluid cells, regardless of fluid fraction. In the simulations, the fluids have been assumed immiscible and incompressible.

4.5 Measurements

Fluctuations of the free surface were acquired in six positions in front of the structure, while a single probe was used to measure wave transmission (not dealt with here, Fig. 10). Along with the horizontal component of the wave force, time series of pressure have been surveyed in 10 positions in front and 10 positions behind the breakwater. The chronogram of the overtopping discharge has been also obtained (Fig. 11) and the wave structure interaction was visually inspected by videos.

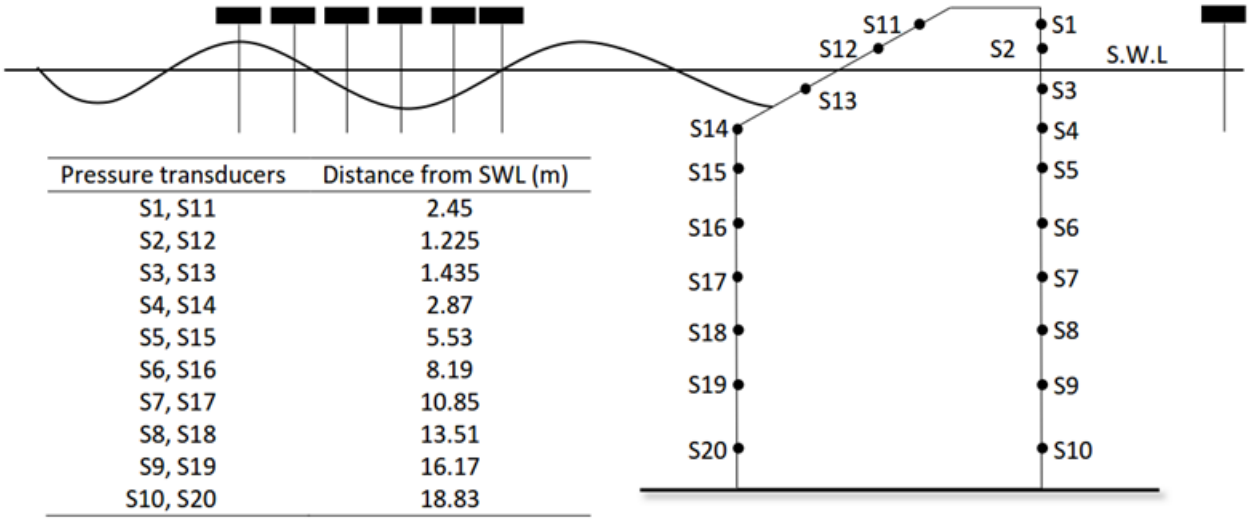

Pressure transducers	Distance from SWL (m)
S1, S11	2.45
S2, S12	1.225
S3, S13	1.435
S4, S14	2.87
S5, S15	5.53
S6, S16	8.19
S7, S17	10.85
S8, S18	13.51
S9, S19	16.17
S10, S20	18.83

Figure 10. Positions of pressure transducers and wave probes

Incident and reflected waves were separated via the Zelt and Skjelbreia (1992) method, which is based on a weighted least square procedure in the frequency domain.

Force and pressure signals have been analyzed separately in front and at the rear of the wall, to capture the effect of wave overtopping.

The rise time of loading events has been calculated as the time interval between the instants corresponding to the 2.5% and 97.5% of the peak magnitude.

Finally, the impulse has been obtained from integration in time.

4.6 Wave Absorption

Unfortunately, FLOW-3D does not allow active wave absorption; however, in this study the presence of a significant overtopping rate limits the effect of undesired re-reflections at the wavemaker. To analyze this point, the horizontal force signal has been divided into two time-segments; the first, $\Delta t1$, corresponds to the time interval for the first wave reaching the structure to travel back to the wavemaker (at the linear phase speed) and reach the breakwater again. The second segment, $\Delta t2$, lasts from the end of $\Delta t1$ to the end of the test.

The Figure 12 compares the standard deviation of the horizontal force signal for $\Delta t1$ and $\Delta t2$ respectively. The graph shows a difference of 4.63% on average, indicating the effect of re-reflections is practically negligible.

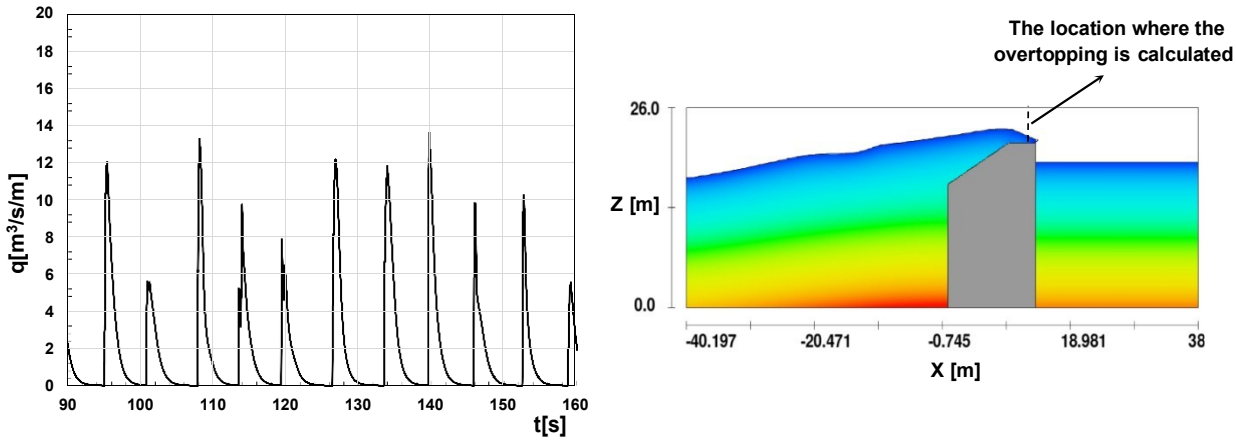

Figure 11. Exmple of overtopping rate time series(left panle) and the location where overtoping is calculated (right panel)

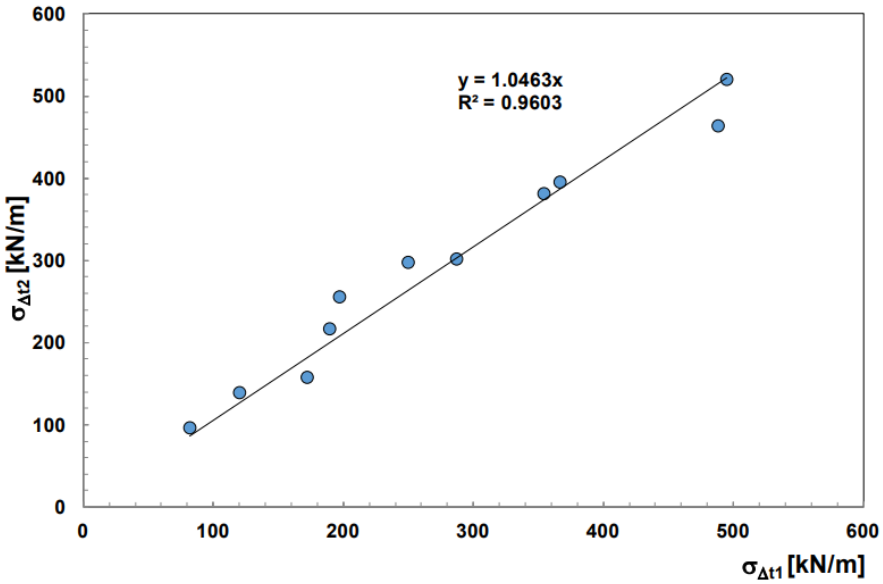

Figure 12. Standard deviation of the horizontal for signal for Δt_1 and Δt_2

5. RESULTS

5.1 Wave shapes and loading features at the front face

5.1.1 Analysis of wave patterns

As argued in the PROVERBS project, nature and magnitude of wave loadings at the outer face of monolithic marine structures may significantly vary depending on the shape of the wave profile.

In this study, three different wave patterns have been recognized and namely:

c) broken waves;
d) plunging breakers;
e) quasi-standing waves.

Broken waves were observed in sea states with high steepness; an example of wave evolution is shown in Figure 13, which refers to the test 1A.

In the picture, the incoming wave is seen to plunge into the water in the neighborhood of the sloping top (frame b); then, the wave reforms and a “secondary plunging jet” detaches from the new crest hitting the wall (frames c and d). Finally, the breakwater is overtopped (frame f).

The resulting force chronogram, displayed in Figure 14, is characterized by a nearly 3Hz oscillation, which likely corresponds to the natural frequency of the flume, excited by the curling down of the wave into the water (low left tip of the figure).

The impact of the “secondary plunging jet” onto the wall produces a sharp peak, with a distribution of pressures (at the instant of maximum force) that is typical of the impact events (e.g. Peregrine, 2003). The measured pressures are significantly larger compared to the predictions of the Takahashi et.al (1994b) method, reported in green in Figure 14 and in Figure 14a. The maximum pressure is underestimated by 80%, whereas an average underprediction of 40% is observed along the wall.

In the case just described, the beneficial effect of the sloping top is seen to be twofold; besides transforming part of the wave slam into vertical force, so reducing the horizontal thrust, the phase lag between the wave pressures along the wall leads the maximum horizontal force to be delayed compared to the impulsive peak. This is clear in Figure 14a, where it is seen that the peak pressure onto the slope is about 11m, but when the maximum force is attained, it is reduced to 8m, i.e. 30% less.

Impact events generated by plunging breakers have been recorded in tests dominated by broken waves, as a particular case in which the curling wave hits the structure instead of plunging into the water.

An example is given in Figure 15, which also refers to the test 1A. The slam of the water tongue leads to impulsive loadings around the transducer S14, i.e. at the junction between the sloping and the upright section (see Figures 16 and 16a).

The Takahashi et al predictions are again largely exceeded; the maximum pressure is underestimated by 90%, with an average underprediction of 50% along the wall. However, the maximum measured pressure is of the order of two times the incident significant wave height, which is far lower than what observed on conventional vertical breakwaters, where relative pressures larger than 10 have been reported (Goda, 1995, Allsop et al., 1996). This occurs because the sloping top constrains the wave front to experience a significant rotation before reaching the structure (curling down), whereas on vertical breakwaters the impact takes place almost frontally (Oumeraci et al., 1993; Calabrese and Buccino, 2000).

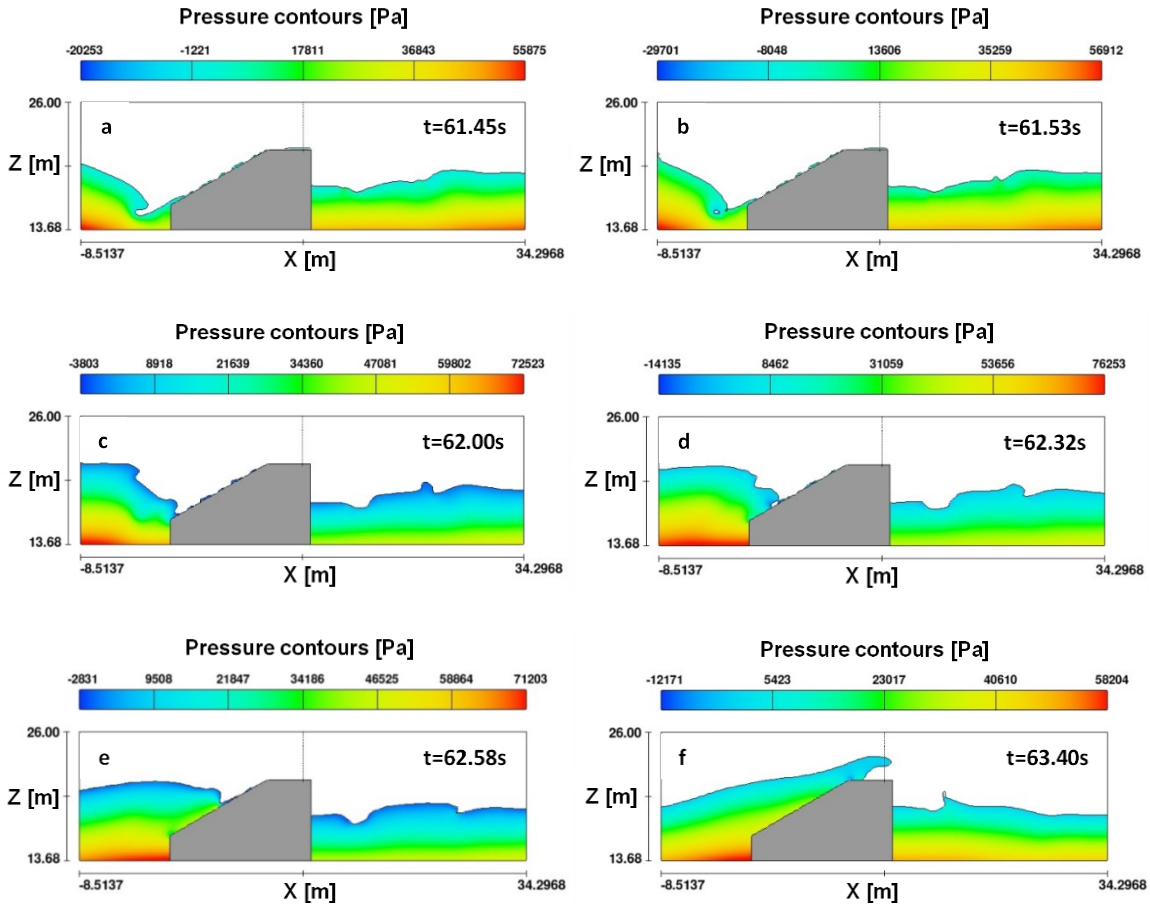

Figure 13. Example of broken wave (Test 1A).

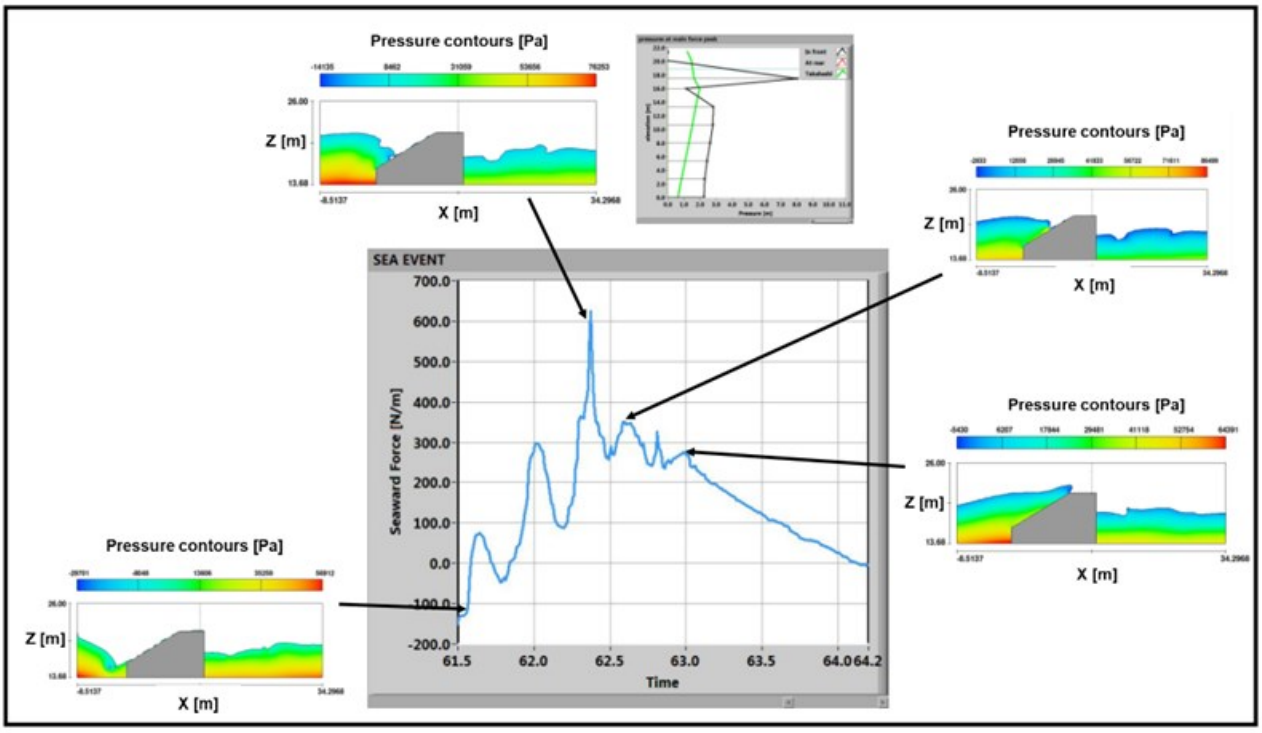

Figure 14. Time history of the horizontal force at the front face of the structure for the event of Figure 6. Time in seconds.

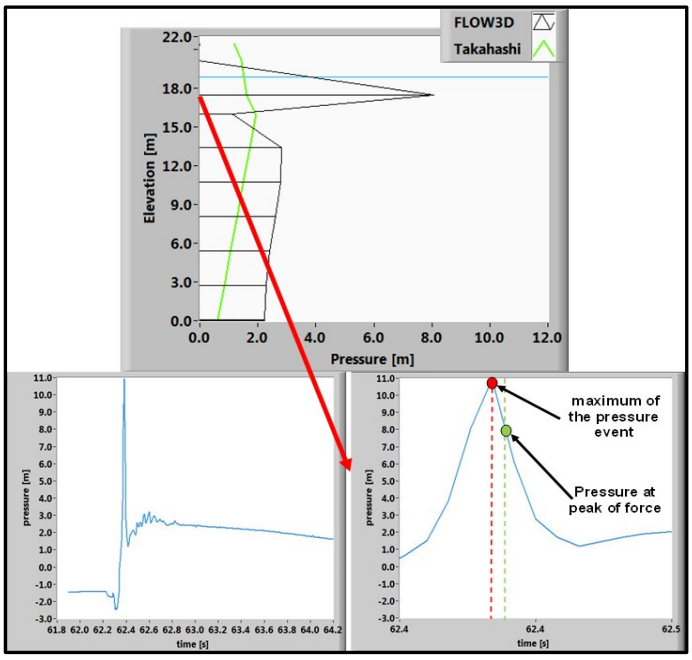

Figure 14a. Upper panel: wave pressure distribution at the force peak of Figure 8; left lower panel: the left the time history of the wave pressure at the location of the maximum in the distribution; right lower panel: zoom of the pressure time history, close to the peak

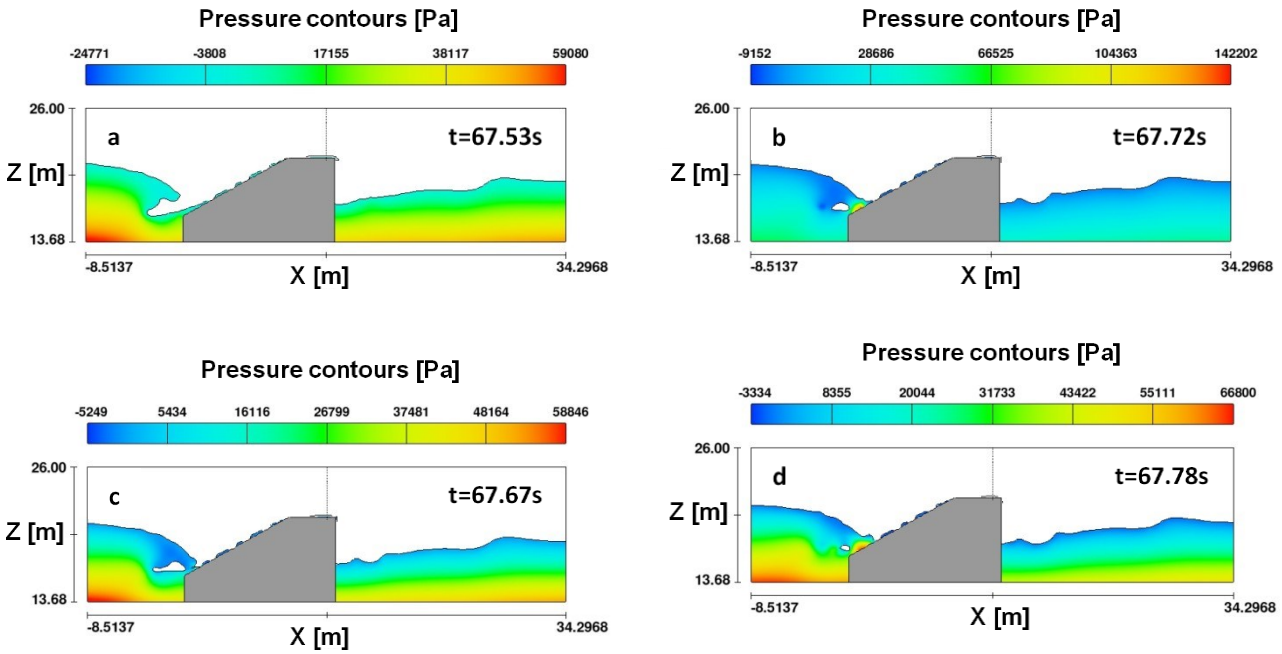

Figure 15. Example of plunging breaker (Test 1A).

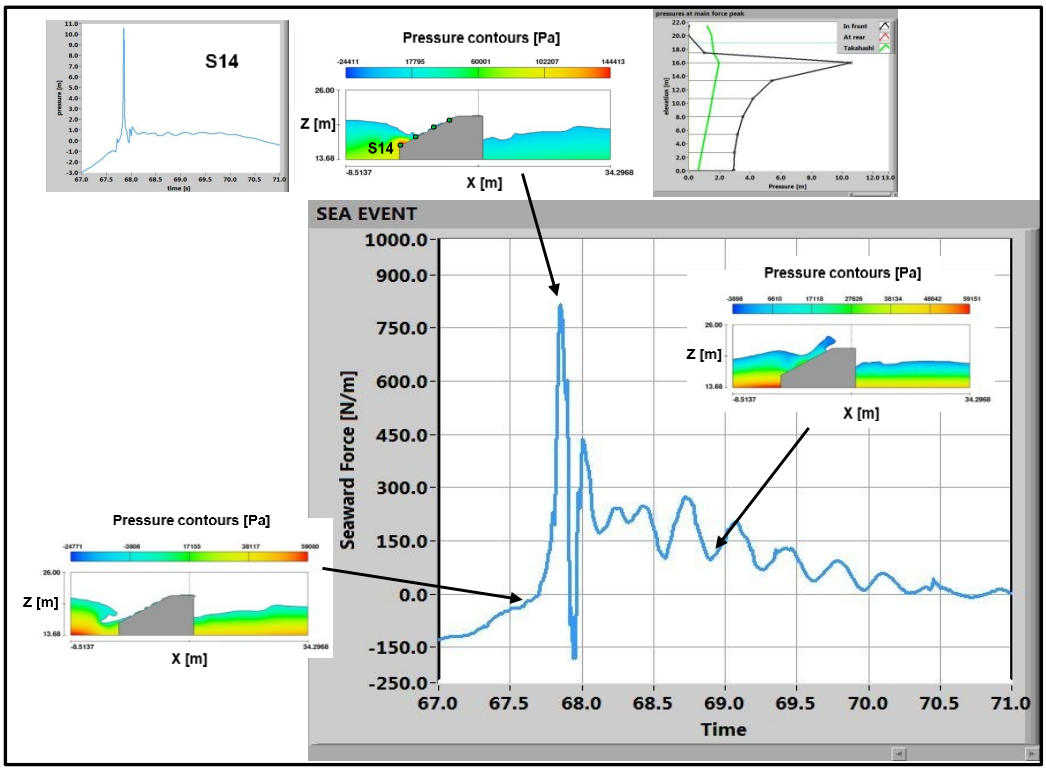

Figure 16. Time history of the horizontal force for the event of Figure 9. Time in seconds

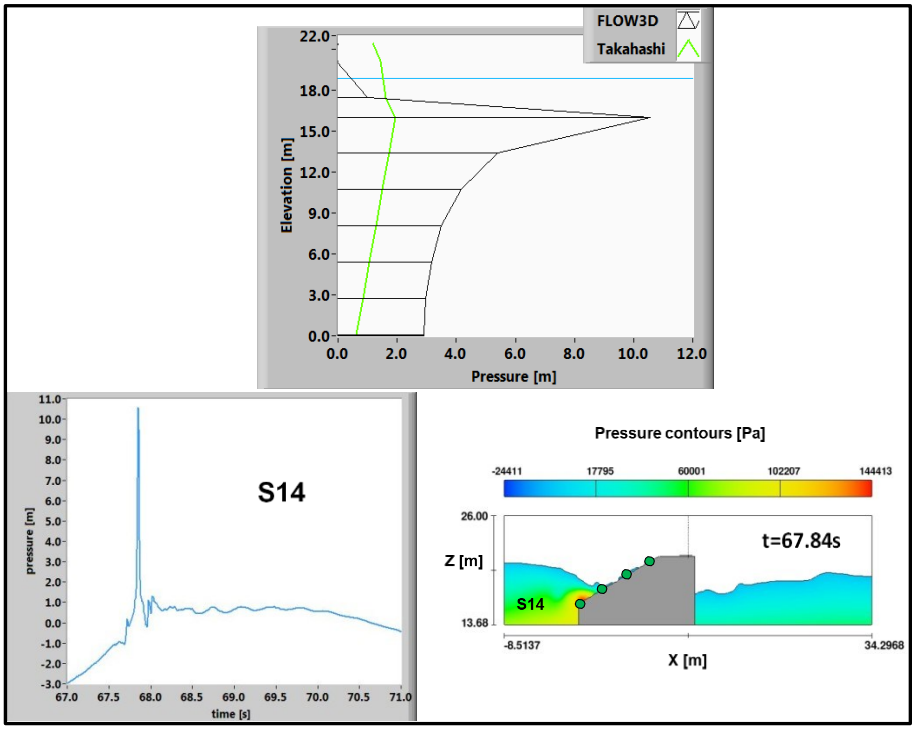

Figure 16a. Upper panel: wave pressure distribution at peak of force for the event of Figure 10. Lower panel: pressure time history at the transducer 14.

With longer periods, quasi-standing waves occur. An example is given in Figure 17, which refers to the test 3B. The wave overtops the structure without impact (frame d), although a secondary plunging jet is seen sometimes to form during the down-rush phase, caused by the abrupt change in the wall profile. As shown in frames a and b, this gives rise to a small impact between the vertical section and the sloping top.

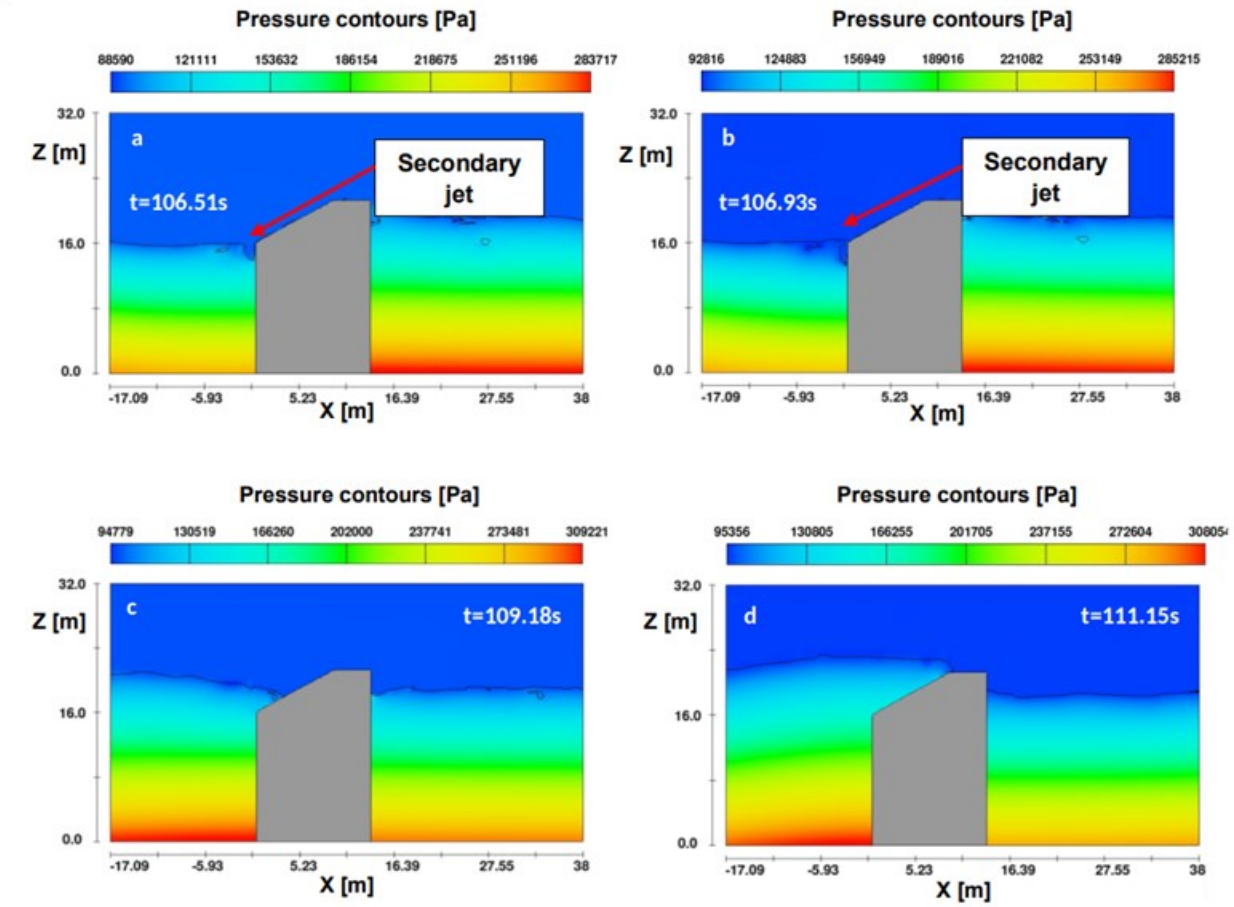

Figure 17. Example of quasi standing wave (Test 3A).

The resulting loading case is basically quasi-static (or pulsating, Figure 18), with the Takahashi et.al method predicting wave pressures at the peak of force rather well. This is shown in the upper part of the Figure 18a; wave pressures are now overpredicted by 30% on average, whereas the maximum pressure is overestimated by 40%.

The small impact described above is actually seen to produce only a fast oscillation of the pressure signals at the transducers S13 and S14 (lower part of Figure 18).

Table 5 reports, for each test, the loading case observed and the value of the maximum nondimensional pressure at the peak of force.

It can be noticed that the impact events, either due to a “direct plunging” or “secondary jet”, generate pressures not exceeding 2.5 times Hm0. No clear effect of the air entrainment has been detected.

This outcome is in a fairly agreement with the results of small scale regular wave physical model tests conducted by Buccino et al. (2015) on a monolithic sloping structure resting on a steep foreshore. The authors measured pressures generated by plunging breakers and found a modal value of 2 times the incident wave height. As mentioned before, this is likely the effect of the inclined outer face, which

forces the incoming wave to rotate before reaching the wall; this impedes a big water mass to be involved in the impact event.

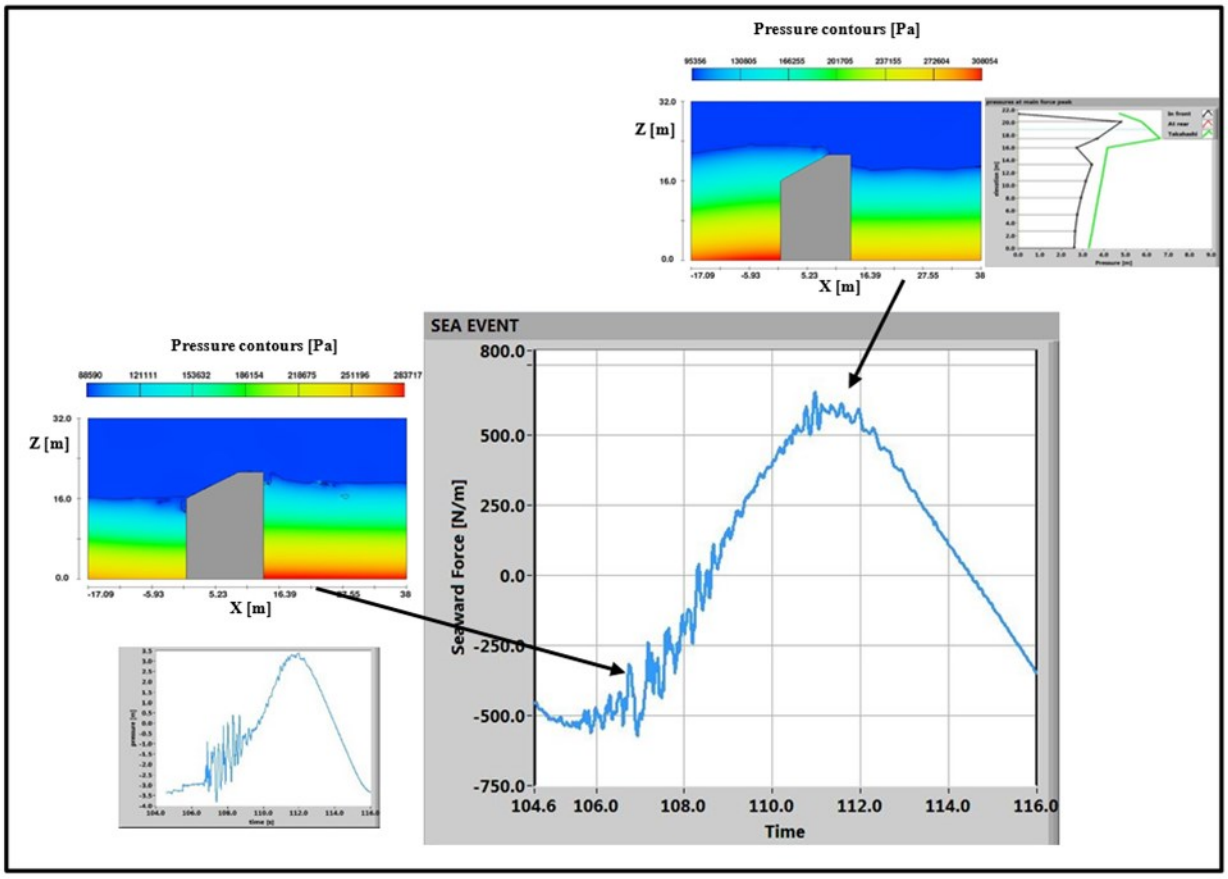

Figure 18. Time history of the horizontal force for the event of Figure 11.

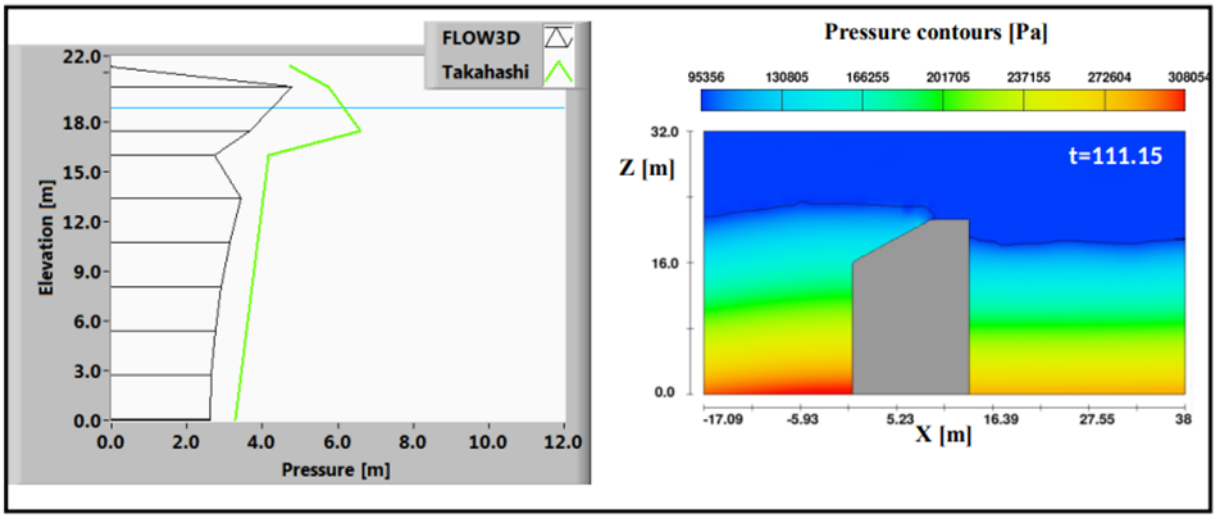

Figure 18a. Wave pressure distribution at the peak of force for the event of Figure 18.

5.1.2. Prediction of loading case and maximum pressure

Within the PROVERBS project two design tools were developed, which allow the prediction of the most probable loading case at simple vertical or vertically-composite breakwaters. One is a parameter decision map (PARM), which uses a few nondimensional variables related to structure geometry, water depth and wave conditions in the nearfield (Oumeraci et al., 1999); the other is a breaking criterion based on two threshold values of the wave steepness Hm0/Lp (Calabrese and Buccino, 2000).

Although the loading cases previously described are some different from those observed onconventional vertical structures, a comparison appears of interest.

Under the hypothesis that the tested sloping top caisson could be assimilated to a simple vertical breakwater, it has been found out the Calabrese and Buccino method to give predictions some more consistent with the observation than PARM (Table 6); this because for simple vertical walls, the latter uses only the wave height to depth ratio as predictive variable, so neglecting the effect of period.

As shown in Figure 19, impact events have been observed for Hm0/Lp included between 0.048 and the limit value at incipient breaking suggested by Kamphuis (1991):

$$H_{m0}/L_p = 0.095 \cdot tanh(2\pi d/L_p) \tag{20}$$

The test 4A, where the waves break rather far from the structure producing no secondary impact, falls above the curve of Eq.(20); conversely, for steepness lower than 0.048 only pulsating loads have been observed. It is also worth to notice that for data not exceeding the Kamphuis limit, the maximum pressure at the peak of force is well predictable as a linear function of the quantity (Figure 20):

$$R_p^* = \frac{R_c}{H_{m0}} \sqrt{\frac{H_{m0}}{gTp^2}} \tag{21}$$

which has been originally introduced by Owen (1980) as a wave overtopping predictor. In practice, data suggest that wave pressure is the more intense the higher wave steepness, since wave breaking tends to occur. However, for a given steepness, though, pressure reduces for low crest freeboards, that is with increasing the overtopping rate.

Table 5. Observed loading cases and maximum pressure at peak of force

TESTCODE	Loading case	max $p/\rho g H_{m0}$
1A	Broken with sec. impact (Fig.6)/plunging breakers	2.186
1B	broken with secondary impact	2.517
1C	broken with secondary impact	2.206
2A	Pulsating	0.992
2B	Pulsating	1.240
2C	Pulsating	1.139
N1	broken with secondary impact	1.680
N2	broken with secondary impact	1.763
3A	Pulsating	0.774
3B	Pulsating	0.945
4A	Broken without secondary impact	1.005

Table 6. Predicted loading cases.

TESTCODE	PARM	Calab&Buc
1A	Pulsating	Broken
1B	Pulsating	Impact
1C	Pulsating	Pulsating
2A	Pulsating	Pulsating
2B	Pulsating	Pulsating
2C	Pulsating	Pulsating
N1	Pulsating	Pulsating
N2	Pulsating	Impact
3A	Impact	Impact
3B	Pulsating	Pulsating
4A	Pulsating	Broken

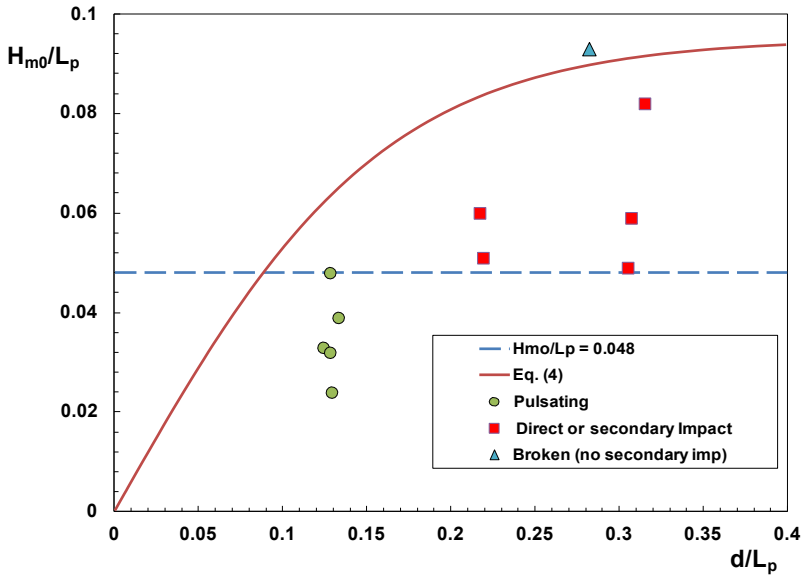

Figure 19. Loading case prediction.

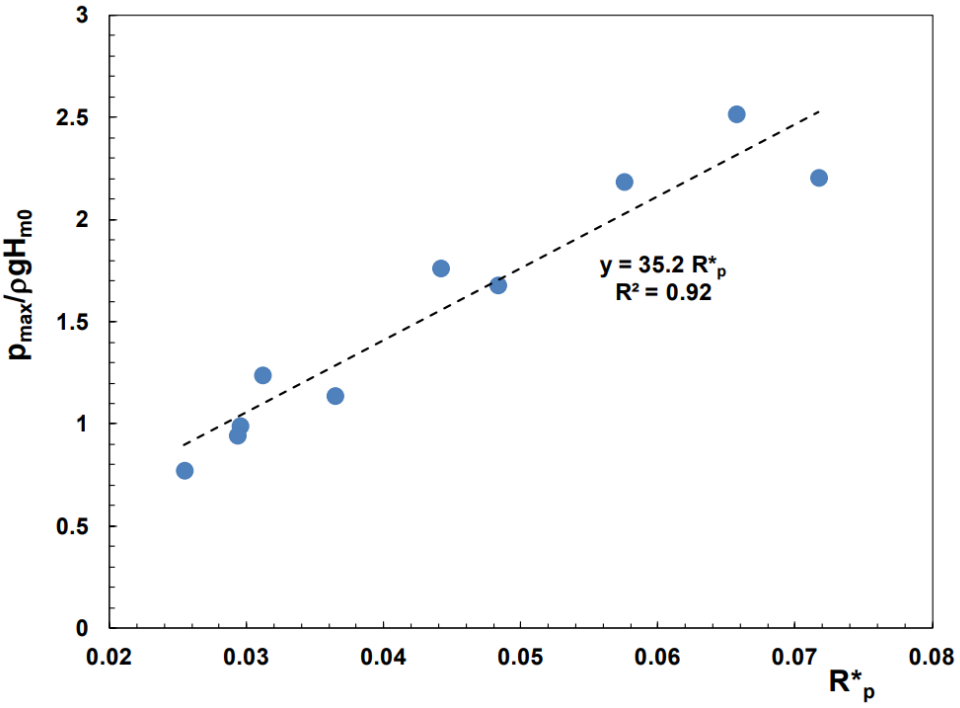

Figure 20. Maximum nondimensional pressure vs. R^*_p.

5.2. Horizontal component of wave force: comparison with literature

As mentioned above, in most of literature studies the only effect of wave overtopping is assumed to be a truncation of the wave pressure distribution at the outer face of the structure.

Accordingly, despite testing overtopped breakwaters also, in Takahashi et al (1994b) no pressure measurements were taken on the rear wall.

In view of this, it has seemed consistent to perform the comparison between predictive models and numerical experiments ignoring, at first, the pressures exerted on the inner face (Subsection 5.2.1 and 5.2.2). Successively, in the Subsection 5.2.3, the effects of wave overtopping are examined in a more detail.

5.2.1 Peak of horizontal force under uprush phase

Figure 21 compares the maximum landward-directed horizontal force measured for each test, to the Takahashi et.al predictions; the latter are obtained using the maximum wave height and the respective period (Hmax and Tmax) as wave parameters.

Most of points exceed the line of perfect agreement, with an average underestimation rate of 79%; additionally, 6 points are underpredicted by a factor larger than 1.4, which is used in the Italian design practice as a safety factor against sliding.

However, these force peaks are mostly generated by breaking waves (e.g. Figures 14 and 16) and, in virtue of their short duration and low impulse, they are not likely to affect the stability of the structure, but rather durability of concrete (Peregrine 2003, Goda, 1986).

With this in mind, the comparison above has been repeated after smoothing the force signals via a second order Savitzky and Golay (1964) filter, with a 0.8s time window (e.g. Figure 22).

As shown in Figure 23, the filtered force peaks compare now quite well with the Takahashi et.al predictions (the average underprediction rate is now 16%) and only two point slightly exceeds the SF=1.4 line.

However, 8 data out 11 are still underestimated; moreover, a trend with relative water depth has been detected, with the amount of underprediction increasing in deep waters (Figure 24).

Previous results do not depend on the inclusion of air in the simulation.

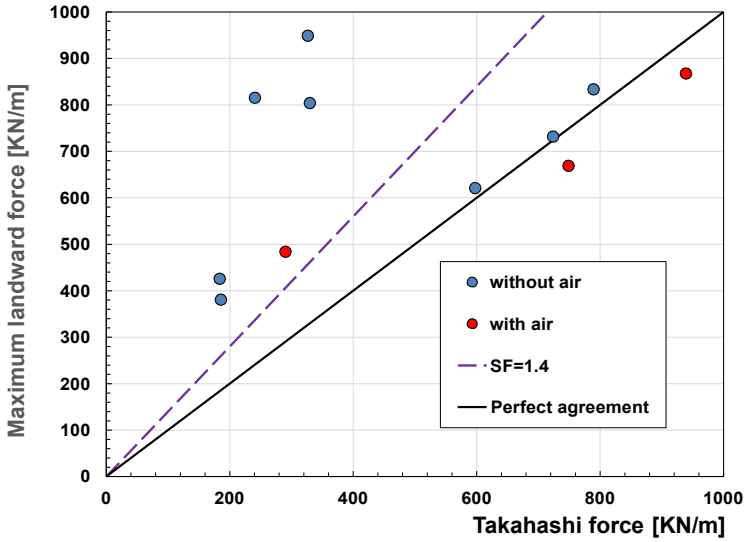

Figure 21. Maximum recorded wave force vs Takahashi et.al 1994b. Only wave loadings on the outer face are considered.

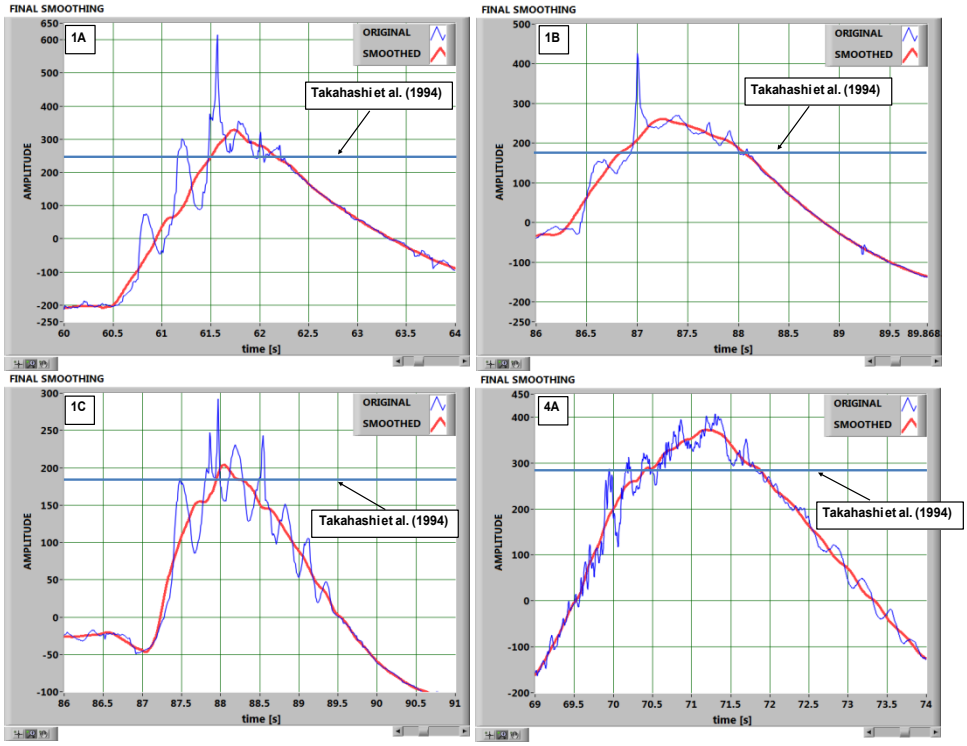

Figure 22. Comparison between Takahashi et al. (1994b) predictions and experimental force maxima after smoothing the breaking induced peaks.

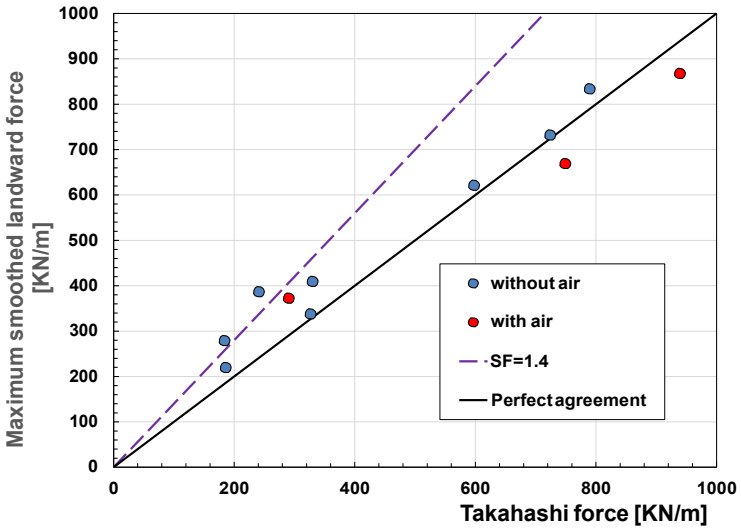

Figure 23. Maximum recorded wave force after smoothing vs Takahashi et.al (1994b)

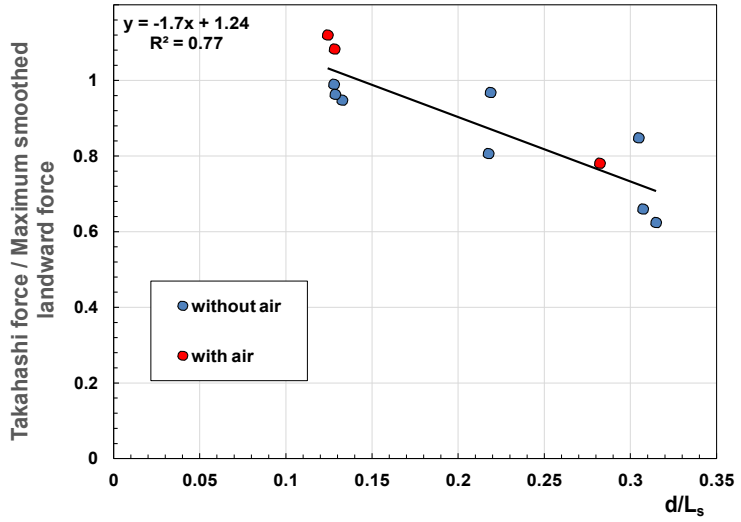

Figure 24. Takahashi et.al safety factor as a function of the relative water depth.

5.2.2 *Horizontal force peak under trough phase*

The maximum seaward-directed horizontal force has been found to exceed the shoreward maximum (after smoothing the breaking peaks) by a factor ranging between 1.1 to 2.1 (1.37 on average, Figure 25).

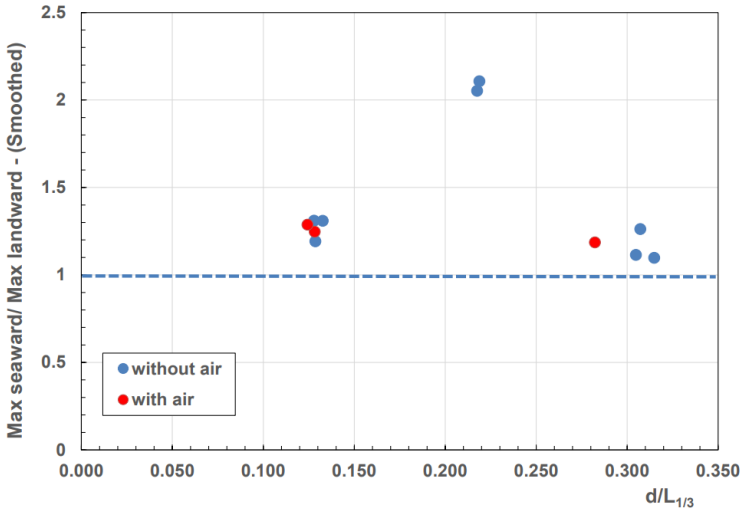

Figure 25. Maximum seaward to maximum landward force ratio vs. relative water depth. Only pressures on the outer wall are considered.

Since no particular suggestions come from the Takahashi et.al work, numerical results have been compared to the methods proposed by Goda (1986) and Saintflou (1928) for traditional vertical-face breakwaters. In both cases, Hmax and Tmax have been employed as wave parameters.

The Figures 26 and 27 show significant underpredictions for the longer waves, although the Sainflou

equation seems to perform slightly better than the Goda model. The average underprediction rate for long waves is around 52% for the Goda method, whereas it lowers to 31% for Sainflou.

These results are qualitatively consistent with the findings of McConell et al. (1999) based on physical model tests on conventional non overtopped vertical breakwaters, although larger underpredictions have been here detected (red broken line Figure 27)

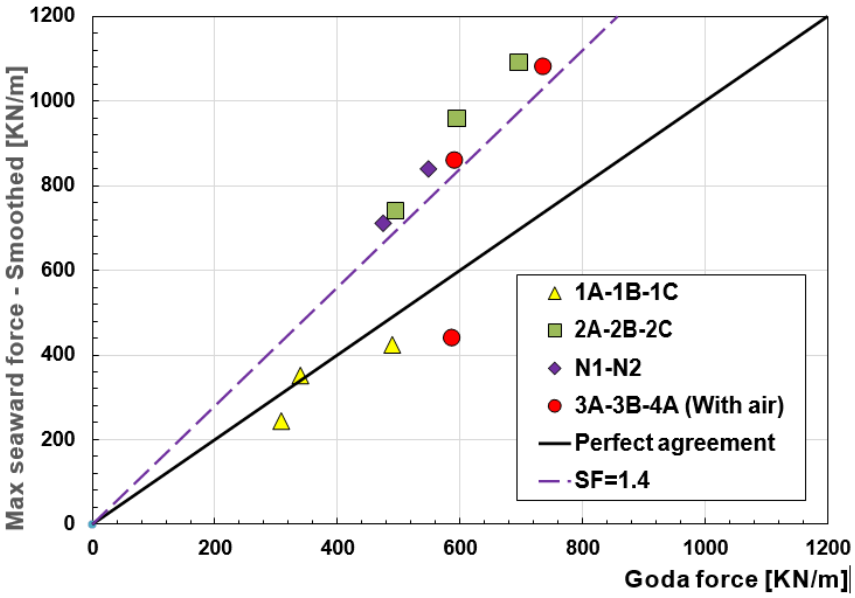

Figure 26. Maximum trough force vs predictions of Goda graphical model

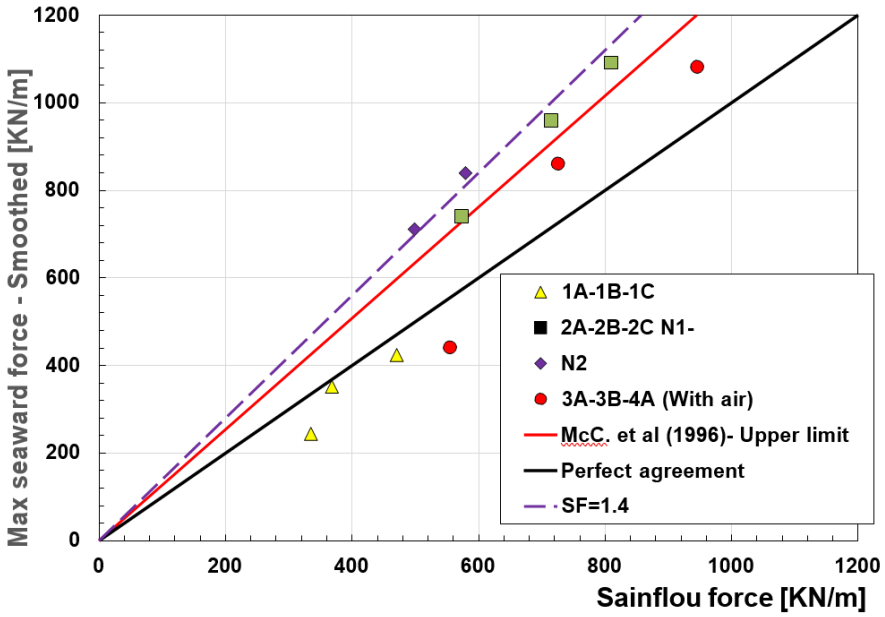

Figure 27. Maximum trough force vs predictions of Sainflou model

5.2.3 *Effect of wave overtopping*

Along with clipping wave pressure distribution at the outer face, wave overtopping also induces loadings onto the inner wall. This produces either a variation of quasi static maxima of wave force, basically due to the phase lag between incident and transmitted waves, or, as shown by Walkden et al. (2001), the occurrence of intense impulsive loadings.

Both these features have been surprisingly little researched so far.

In the following, only “quasi static effects” are discussed, whereas impact loadings are analyzed in Buccino et al.(2019) .

For the analyses discussed below, wave force chronograms have been first re-computed including rear pressures; then, they have been smoothed using the Savitzky and Golay filter (as employed in the Section 5.2.1) to retain only the pulsating part.

It has been found out that wave overtopping amplifies both the seaward and the landward horizontal force peaks; as shown in Figure 28, when the maximum landward-force is attained (upper panel), negative pressures take place at the inner wall and vice versa.

However, Figure 29 suggests the amplification factor to be negligible for trough loads (1.05 on average, panel b), whereas for the landward-directed force it reaches 1.16.

With including the overtopping loadings, the ratio between the maximum force under trough and the maximum force under crest lowers from 1.37 on average (Figure 19) to nearly 1.20.

However, all data under wave crest are underpredicted by the Takahashi et al. formula. The mean underprediction rate is now 22%, compared to the 16% detected in Figure 23.

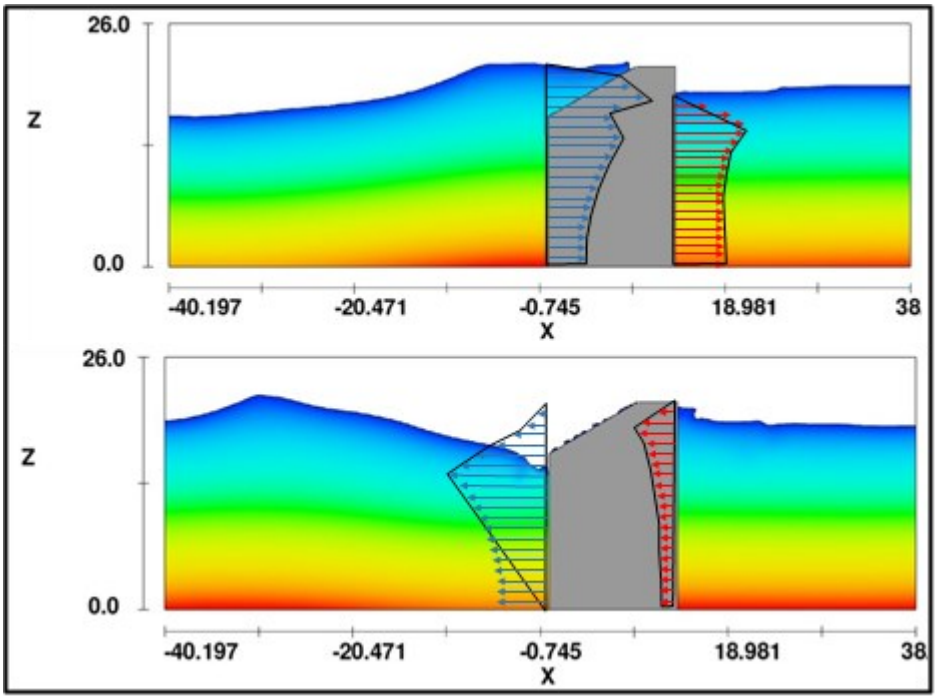

Figure 28. Wave pressure distribution at the peaks of force for test 2B. Upper panel: crest phase; Lower panel: trough phase.

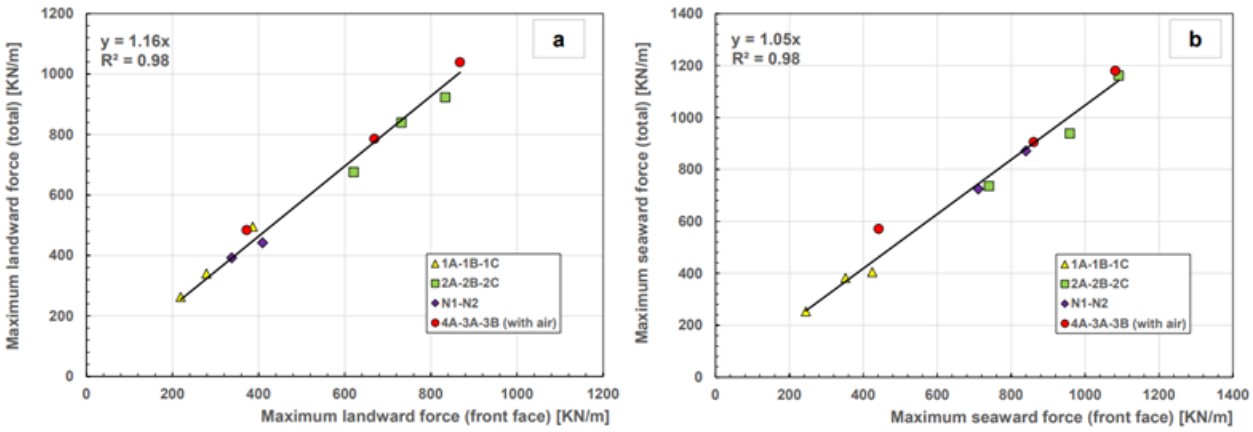

Figure 29. Force peak calculated at the front face vs total force peak including loadings generated by wave overtopping. (a) Landward directed (crest); (b) Seaward directed (trough).

5.3 Approximate sliding force

As the wave force under trough generally exceeds the wave force under crest, and since the presence of dynamic pressures at the inner wall (Figure 28) invariably alters the regime of uplifts, it is rather difficult to predict which wave phase (whether crest or trough) may be the most critical for structure stability.

To have a deeper insight of this issue, the sliding force, SL, should be more appropriately considered. The latter represents the total shear the structure has to withstand (by its weight) to prevent sliding on the bottom.

Neglecting the wave loadings exerted on the caisson roof, SL can be defined as follows (Figure 30):

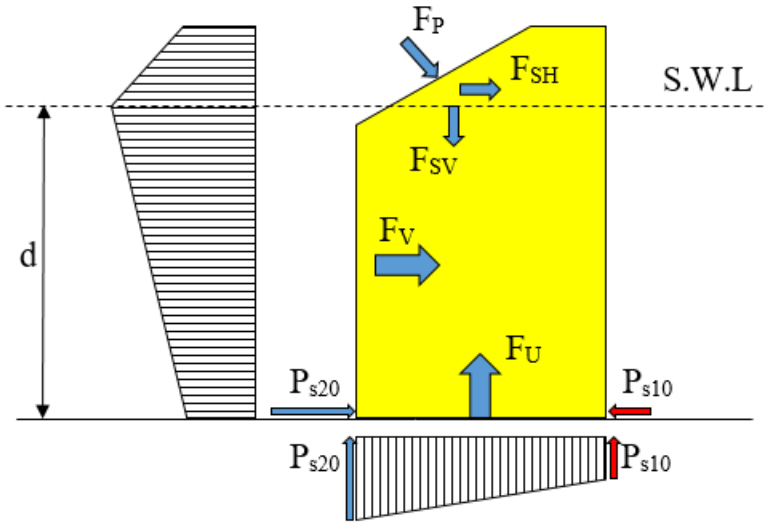

Figure30. Definition sketch for sliding force.

$$S_L = F_H + \mu(F_{uplift} - F_{sV}) \tag{22}$$

In which:

- $F_H$is the horizontal force including the overtopping effects;
- $F_{uplift}$is the uplift force acting at the bottom;
- $F_{sV}$is the vertical component of the wave force at the sloping top;
- μ is the structure-bottom friction factor.

In the present study, due to the lack of measurements for uplifts, only an approximate sliding chronogram can be calculated, in which the distribution of pressure beneath the structure is assumed trapezoidal in all instants (Figure 30). In practice, that means to set:

$$F_{uplift} \cong 0.5 \cdot (p_{S20} + p_{S20}) \cdot b \tag{23}$$

where pS20 and pS10 are the pressure signals at the transducers 20 and 10 respectively (Figure 10), and b

indicates the caisson width.

A sample of sliding signal (after smoothing) is shown in Figure 31, whereas Figure 32 compares, for each test, the maximum positive (landward-directed) and the maximum negative (shoreward directed) peaks. The graph indicates that for the larger periods the structure would tend to slide seaward, being the negative peak up to twice the positive one .

In practice, under wave crest the presence of negative dynamic pressures on the rear wall (see upper panel of Figure 28) increases FH, but reduces uplifts.

On the other hand, under a wave trough, both the previous components (FH and $Fuplift$) are enhanced, so that the seaward sliding peak is amplified by wave overtopping.

Furthermore, it is worth noticing that since the sloping top extends below the swl, it tends to favor the sliding under trough, as the vertical component of the negative wave pressures is upward directed (lower panel of Figure 28).

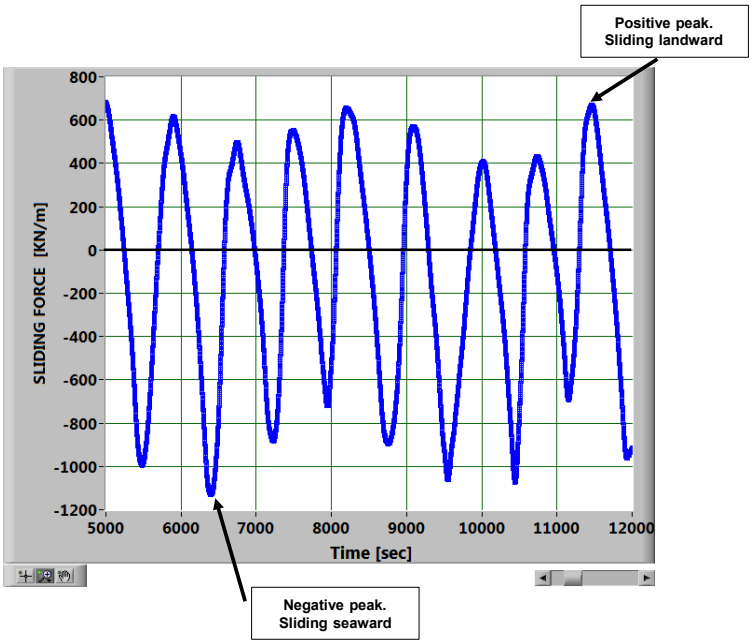

Figure 31. Example of sliding force signal (smoothed).Test 2A

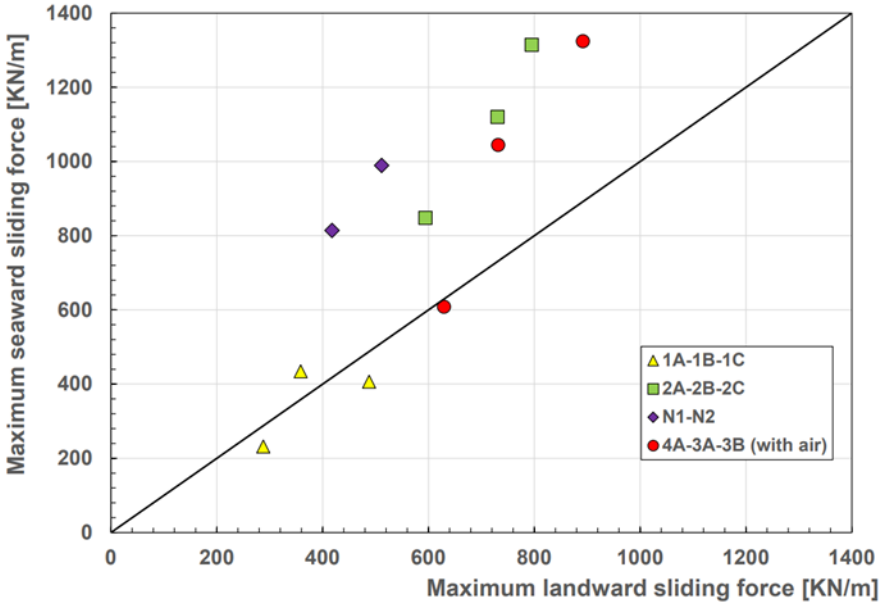

Figure 32. Maximum landward sliding force vs maximum seaward (Smoothed signals)

The Figure 33 shows the comparison with literature models. Analogously to what observed for FH, the Takahashi et al. method predicts up to a certain extent the measurements, although some underpredictions for the shorter waves has been detected (average underprediction rate 42%) ; on contrary, under a wave trough, the Sainflou formula exhibit larger underestimations (60% on average), which may render design process rather uncertain.

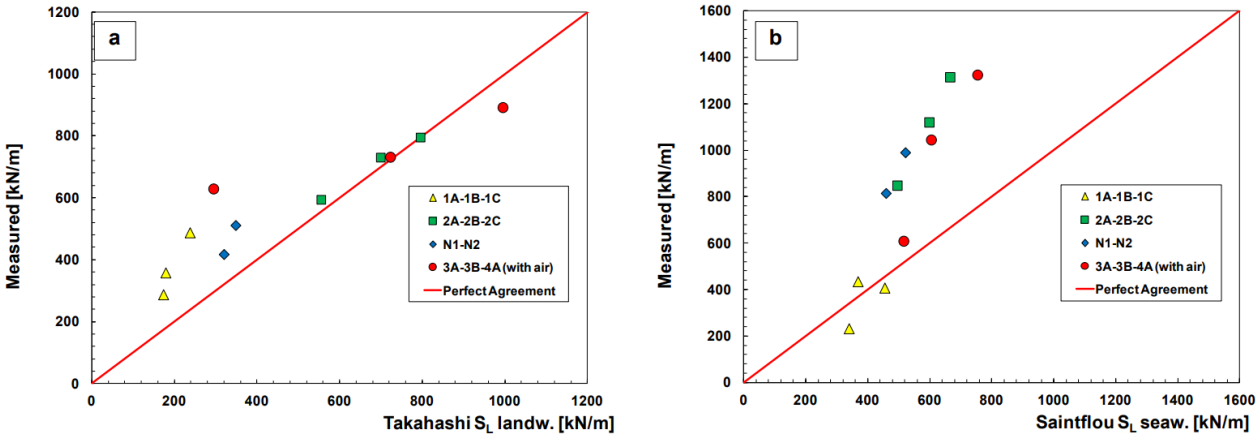

Figure 33. Peaks of sliding force vs. literature models. Panel a) Takahashi et al. (crest phase). Panel b) Saintflou formula (trough phase).

5.4 The use of the Linear Thrust Parameter

None of the literature methods have been found to be plenty satisfactory in predicting present data; this is especially true for trough conditions, which, on the other hand, have been shown to be crucial for the structure stability. Hence, an alternative approach is here tested, namely that introduced by Buccino et al. (2015) in the frame of the experimental study mentioned in the Subsection 3.2.

In analyzing the behavior of SSGs subject to severe overtopping, the authors proposed the following linear formula to calculate the horizontal component of the (quasi-static) wave force under crest phase:

$$F = K \cdot \rho g L_{TP} d h_c \tag{24}$$

where, beyond the quantities already introduced, hc represents the structure height.

In the Eq.(24), LTP is the linear thrust parameter, i.e. the ratio between the linearized maximum momentum flux due to the incoming waves and the hydrostatic force corresponding to the still water level d.

Basically, Buccino et al. (2015) considered the ratio between the maximum value (over a wave period) of the cross-shore component of the incident wave momentum flux at the toe of the structure, and the corresponding hydrostatic still water thrust:

$$L_{TP} = max_{t \in T} \frac{\int_{-d}^{\eta} (p + \rho g z + \rho u^2) dz}{0.5 \rho g d^2} \tag{25}$$

In the Eq.(25), η is the free surface, z is the vertical coordinate (positive upwards), u is the cross-shore wave velocity, ρ is the water density and g is the gravity acceleration. By using the linear wave theory, and retaining only the first order terms, one gets:

$$L_{TP} = \frac{H \tanh(kd)}{d \quad kd} \tag{26}$$

which is a fully linearized and slightly modified form of the momentum flux parameter originally

introduced by Hughes (2004; see also Buccino et al., 2018) Note that L_{TP} coincides with the wave height to depth ratio *(H/d)* in shallow water.

Altogether, the Eq.(24) establishes a simple proportionality between wave force and maximum wave momentum flux, via the empirical coefficient *K*, which Buccino et al. (2015) reasoned to be of the order of 1. The retaining of the first order terms only is legitimized by the low crest of the structure.
For the case of SSG, a value of $K = 0.77$ has been estimated, based on regular wave physical model tests; despite a very good R^2 statistics was found (0.95), the authors warned that some (small) non linear effects could exist.
In this paper, the Eq. (24) has been used to predict both the landward and the seaward horizontal force maxima, where the overtopping effects are included; according to the previous sections, H_{max} and T_{max} have been employed as wave parameters.
As shown in Figure 33, the method performs rather well for the landward peak, for which the same *K* as in Buccino et al. (2015) has been found and a very good R^2 statistics (0.92). On the other hand, the prediction power drops a little under trough conditions, although the R^2 still remains relatively high.

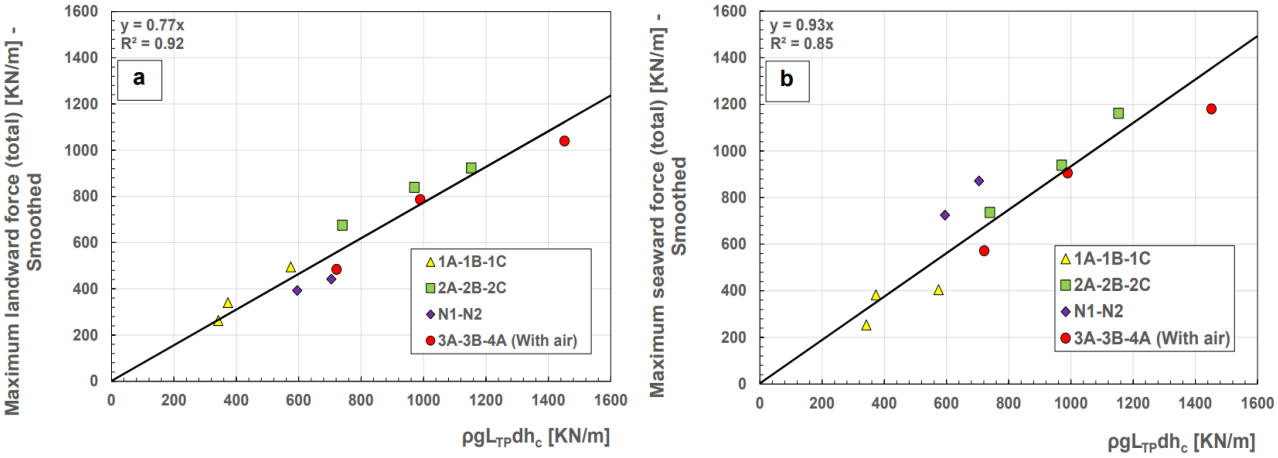

Figure 34. Peaks of horizontal force, vs. L_{TP} approach. Panel a) crest phase. Panel b) trough phase

Finally, an attempt has been conducted to use the L_{TP} method for the prediction of the (approximate) sliding force maxima. To this purpose, a simplified distribution of pressures has been hypothesized, which is uniform on the front face and triangular at the bottom. Accordingly, the magnitude of the front pressure, p_{front}, and the maximum uplift, $p_{u,max}$, is assumed to be:

$$p_{front} = p_{u,max} = K \cdot \rho g L_{TP} d \qquad (11)$$

where the values of K are those obtained from the Figure 29.

In spite of the simplification introduced, the proposed approach still allows good predictions of the experimental data (Figure 35); again, the estimates under crest are rather efficient, although some non-linear effects are visible. The model is less accurate (but still reasonable) under trough, where the hypothesis of uniform distribution of the front pressures becomes quite questionable.
Table 7 reports some reliability indexes.

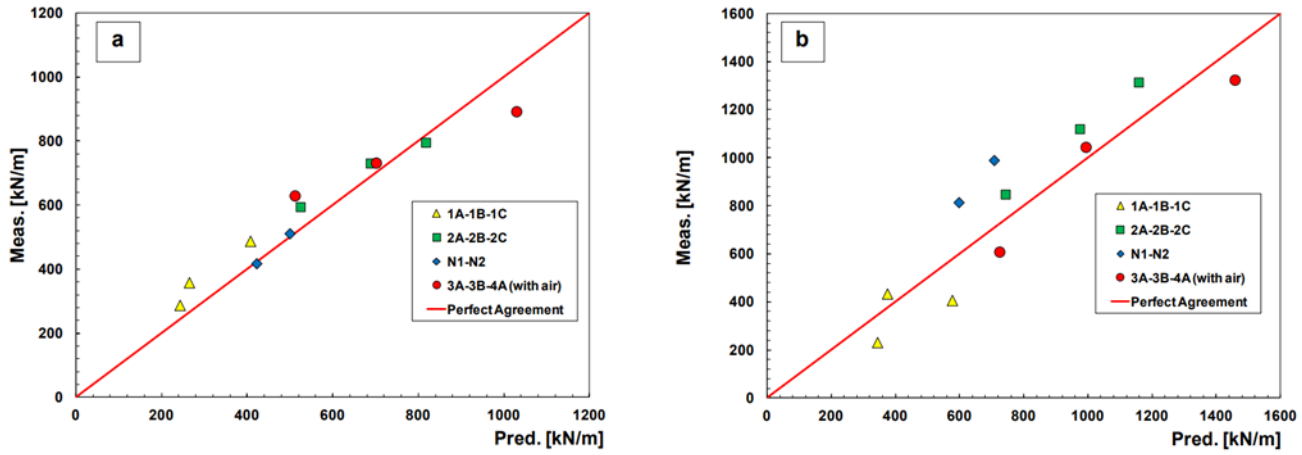

Figure 35. Peaks of (approximate) sliding force, vs. L_{TP} approach. Panel a) crest phase. Panel b) trough phase

Table 7. Reliability indexes for the linear momentum flux approach.

	K	R^2	$\sigma\ [\frac{kN}{m}]$	Max [meas/pred]	Min [meas/pred]
max landward horiz. force peaks	0.77	0.92	69.16	1.18	0.82
max seaward horiz. force peaks	0.93	0.85	115.90	1.33	0.76
max landward sliding force	0.77	0.85	69.07	1.33	0.85
max seaward sliding force	0.93	0.83	148.5	1.33	0.7

4 SUMMARY AND CONCLUSIONS

A set of 11 full scale random wave CFD experiments have been conducted, to deepen the knowledge on the loading process at sloping top caissons subject to significant wave overtopping. The commercially available software FLOW-3D has been used, which numerically solves the Reynolds Averaged Navier Stokes Equations using the finite-difference method with a stationary Cartesian grid. As for the turbulence closure, the ReNormalized Group (RNG) extension of the k-ε model has been selected, which is particularly suited to describe the wave evolution in the neighborhoods of the breaking point.
The structure employed had a relative crest freeboard, Rc/Hm0, ranging from 0.4 to 0.8, whereas the
relative water depth, d/Lp, was included between 0.12 and
0.31.
Despite the limitedness of data, a number of interesting items have been discussed with respect to:

- loading case occurring at the structure;
- global stability conditions;
- predictability of wave actions

As far as the loading cases are concerned, although testing very steep waves, giving rise to impact conditions, the maximum pressure at the instant of the maximum force has been observed not to

exceed 2.5 times the incident significant wave height, i.e. far less than what measured on conventional vertical face breakwaters.
This finding is consistent with the results of physical model tests conducted by Buccino et al. (2015) and is essentially caused by the presence of the sloping top, which constraints the breaking front to a big rotation before hitting the wall. Additionally, the discontinuity of the wall profile produces a phase lag between the pressure signals, which leads the instant of maximum force not to coincide with the instant of maximum impulsive pressure.

Regarding the global stability, it has been found out that since wave overtopping leads to a significant reduction of loadings under wave crest, trough conditions become crucial to the structural response. This is especially true for long waves, with relative water depth included between 0.1 and 0.2.

This is consistent with the case history published in 1994 by Oumaraci, who reported the cases of 5 real vertical breakwaters (out 14 examined), which failed seaward after experiencing severe overtopping. In the four cases where wave data were available (Valencia, Catania, Algiers, Niigata), the relative crest freeboard was included between 0.64 and 1.07, whereas the relative water depth ranged between 0.08 and 0.17, indicating long waves similar to those employed in this study.
In this respect it is worth to emphasize that differently from what argued by Walkden et.al, present data suggests that seaward failure of overtopped breakwaters is not necessarily related to the occurrence of impact forces onto the rear face (the sliding signals here analyzed have been here previously smoothed); rather, significant overtopping reduces the landward force peaks compared to non-overtopped structure, making the seaward peaks comparatively larger and crucial to the stability.

It has been then observed that wave actions under crest are reasonably predicted by the Takahashi et al. method, although a certain trend at underestimating data has been detected, especially for short periods; this would confirm the previous findings of Vicinanza and Frigaard (2009).
However, large underpredictions have been found for the trough phase, where no specific method exists but those valid for conventional vertical phase breakwaters.
In view of this result, an alternative predictive approach has been tested, which assumes a simple proportionality law between wave force and peak of linear wave momentum flux.
The method proved to be rather efficient under wave crest and this appears very interesting in virtue of the simplicity of calculations.
Under wave trough, the momentum flux approach still remains an useful prediction tool, producing a remarkable improvement compared to the existing methods, such as the Sainflou formula. Neverthless, the quality of estimates lowers a little; this occurs mainly because some of the assumptions the method relies on are no longer verified; this includes the uniform distribution of pressures along the entire outer face of the structure and the neglecting of the hydrostatic thrust above the trough, which is of order of H2
On the whole, this research has suggested that significant gaps still exist about the global features of
loadings exerted by waves on non conventional monolithic breakwaters and that a supplementary research effort is needed, to reduce the degree of uncertainty that affects the design process.

REFERENCES

Allsop, N.W.H., Vicinanza, D., Calabrese, M., Centurioni, L., 1996. Breaking wave impact loads on vertical faces. In: Proceedings of the 6th International Conference ISOPE, Los Angeles, published by ISOPE, Golden, Colorado, USA, vol. 3, pp. 185–191.

Antonini, A., Archetti, R., Lamberti, A., 2017. Wave simulation for the design of an innovative quay wall: The case of Vlorë Harbour. NATURAL HAZARDS AND EARTH SYSTEM SCIENCES. vol. 17(1), p. 127-142. ISSN: 15618633. doi: 10.5194/nhess-17-127-2017.

Antonini, A. Lamberti, A., Archetti, R., Miquel, A.M.,2016. CFD investigations of OXYFLUX device, an innovative wave pump technology for artificial downwelling of surface water. Applied Ocean Research. Volume 6, Pages 16-31.

Bradford, S.F., 2000. Numerical simulation of surf-zone dynamics. J. Waterway, Port, Coastal, Ocean Eng., 2000, 126(1): 1-13.

Buccino, M., Vicinanza, D., Dalerno, D., Banfi, D., Calabrese, M., 2015. Nature and magnitude of wave loadings at Sea-wave Slotcone Generators. Ocean Engineering. 95, 34-58.

Buccino, M., Dentale, F., Salerno, D., Contestabile, P., Calabrese, M., 2016. The Use of CFD in the Analysis of Wave Loadings Acting on Seawave Slot-Cone Generators. Sustainability, MDPI.

Buccino, M., D'Anna, M., Calabrese, M., 2018. A study of wave reflection based on the maximum wave momentum flux approach. Coastal Engineering Journal, 60(1), 1-21.

Buccino, M., Daliri, M., Dentale, F., Calabrese, M., 2019. CFD Experiment on a Low Crested Sloping Top Breakwater. Part 2: Analysis of Plume Impact. Ocean Engineering 173, 345-357.

Calabrese, M., Buccino, M., 2000. Wave impacts on vertical and composite breakwaters. In: Proceedings of the 10th International Conference ISOPE, Seattle.

Calabrese, M. Allsop, N.W.H. Buccino, M., 2000. Effect of random multidirectional wave fields on wave loads on vertical and composite breakwaters. In: Proceedings of the 27th International Conference on Coastal Engineering, vol.2. Sydney, Australia, 16–21 July 2000, pp. 1710–1723.

Cooker, M.J., Peregrine, D.H., 1990. Violent water motion at breaking wave impact. Proc. of 22nd International Conference on Coastal Engineering.

Cuomo, G., Allsop, W., Takahashi, S., 2010. Scaling wave impact pressures on vertical walls. Coast. Eng. 57, 604–609.

Dentale, F, Donnarumma, G, Pugliese Carratelli, E, 2014a. Simulation of flow within armour blocks in a breakwater. J. Coast. Res. 2014, 30, 528–536.

Dentale, F, Donnarumma, G, Pugliese Carratelli, E, 2014b. Numerical wave interaction with Tetrapods breakwater. J. Naval Arch. Ocean Eng. 2014, 6, 800–812.

Flow Science Inc. , 2009. Suite Flow 3D; Flow Science Inc.: Santa Fe, Mexico.

Gaeta, M.G., Lamberti, A. (2015). The role of air modeling on the numerical investigation of coastal dynamics and wave-structure interactions (2015) Computers and Fluids, 111, pp. 114-126.

Goda, Y., 1986. Random sea waves and Engineering applications. University of Tokyo Press.

Goda, Y., 1995. Japan's design practice in assessing wave forces on vertical breakwaters, Wave forces on inclined and vertical wall structures. ASCE p. 402.

Hattori, M., Arami, A., 1992. Impact breaking wave pressures on vertical walls. Proc. of 23rd International Conference on Coastal Engineering.

Hirt, C. W., and Nichols, B. D., 1981. Volume of fluid (VOF) method for the dynamics of free boundaries. J. Computational Phys., 39, 201–225.

Hirt, C. W., and Sicilian, J. M., 1985. A porosity technique for the definition of obstacles in rectangular cell meshes. Proc., 4th Int. Conf. on Ship Hydrodynamics, National Academy of Science, Washington,D.C.

Hughes, S.A., 2004. Wave momentum flux parameter: a descriptor for nearshore waves. Coast. Eng. 51 (11–12), 1067–1084.

Jun, J., Meng, B., 2011. Computation of wave loads on the superstructures of coastal highway bridges. Coastal Engineering 38(2011), 2185-2200.

Kamath, A., 2015. CFD based Investigation of Wave-Structure Interaction and Hydrodynamics of an Oscillating Water Column Device. Thesis for the degree of Philosophiae Doctor. Norwegian University of Science and Technology. December 2015.

Kamphuis, J.W., 1991. Incipient wave breaking. Coastal Engineering 15, 185–203.
Kirkgoz, M.S., 1991. Impact pressure of breaking waves on vertical and sloping walls. Ocean Engineering, vol 18. Elsevier.
Larsen, B.E., Fuhrman, D.R., 2018. On t he over-product ion of turbulence beneath surface waves in Reynolds – averaged Navier–Stokes models. J. Fluid Mech . (2018), vol. 853, pp. 419–460.
Launder, B.E., Spalding, D.B., 1974. The numerical computation of turbulence flows. Computer methods in applied mechanics and engineering, 3(2):269-289.
Lundgren, H., 1969. Wave shock forces: an analysis of deformations and forces in the wave and in the foundation. Proc. Symp. on Research in Wave Action. Delft Hydraulics Lab, Delft, the Netherlands.
Miquel, A.M., Kamath, A., Chella, M.A., Archetti, R., Bihs, H., 2018. Analysis of different methods for wave generation and absorption in a CFD-based numerical wave tank. Journal of Marine Science and Engineering, 6 (2), art. no. 73.
McConnell KJ, Allsop NWH and Flohr H (1999) Seaward wave loading on vertical coastal structures. In Coastal Structures '99 (Losada IJ (ed.)). Balkema, Rotterdam, the Netherlands, pp. 447–454.
Oumeraci, H. (1994). Review and analysis of vertical breakwater failures-lessons learned. Coastal Engineering,22 (1994) 3-29.
Oumeraci, H., Klammer, P., Partenscky, H.W., 1993. Classification of Breaking Wave Loads on Vertical Structures. Journal of Waterway Port Coastal and Ocean Engineering 119(4).
Oumeraci, H., Allsop, N.W.H., De Groot, M.B., Crouch, R.S., Vrijling, J.K., 1999. Probabilistic design tools for vertical breakwaters. Balkema, Rotterdam the Netherlands.
Owen, M. W., 1980. Design of seawalls allowing for wave overtopping. Rep. EX 924b, Hydraulics Research Station, Wallingford, England.
Peregrine, D.H., 2003. Water-wave impact on walls. Ann. Rev. Fluid Mech. 35, 23–44.
Saad, Y., 1996. Iterative Methods for Sparse Linear Systems. Soc. for Industrial and Applied Mathematics.
Sainflou, G., 1928. Essai sur les digues maritimes, verticales, Annales Ponts et Chaussées, Vol. 98, No.4.
Savitzky A., Golay, M.J.E. (1964). Analytical Chemestry, vol.36, 1627-1639.
Takahashi, S., Tanimoto, K., Shimosako, K., 1994a. Dynamic response and sliding of breakwater caissons against impulsive breaking wave forces. Workshop on wave barriers in deep waters, port and harbor research institute, Yokosuka.
Takahashi, S., Hosoyamada, S., Yamamoto, S., 1994b. Hydrodynamic characteristics of sloping top caissons. Proceedings of International Conference on HydroTechnical Engineering for Port and Harbor Construction, 1. Port and Harbour Research Institute, Japan, pp. 733–746.
Tanimoto, K., Kimura, K., 1985. A hydraulic experiment study on trapezoidal caisson breakwaters. Port and Harbour Research Institute, Yokosuka, Japan (Technical Note No. 528).
Ting, F. C. K., and Kirby, J. T. 1994. Observation of undertow and turbulence in a laboratory surf zone. Coast. Engrg., 24, 51–80.
Vicinanza, D., Frigaard, P., 2009. Wave pressure acting on a seawave slot-cone generator. Coast. Eng. 55, 553–568.
Vicinanza, D., Margheritini, L., Kofoed, J.P., Buccino, M., 2012. The SSG wave energy converter: performance, status and recent developments. Energies 5 (2), 193–226.
Vicinanza, D, Dentale, F, Salerno, D, Buccino, M, 2015. Structural response of Seawave Slot-Cone Generator (SSG) from Random Wave CFD simulations. Proceedings of the International Offshore and Polar Engineering Conference (ISOPE 2015). 2015-January, pp. 985-991.
Walkden, M.J., Wood, D.J., Bruce, T., Peregrine, D.H., 2001. Impulsive seaward loads induced by wave overtopping on caisson breakwaters. Coastal Engineering 42 2001 257–276.
Yakhot, V., Orszag, S. A., Thangam, S., Gatski, T. B., and Speziale, C.G., 1992. Development of turbulence models for shear flows by a double expansion technique. Phys. of Fluids A, 4, 1510-1520.Zelt, J.A., Skjelbreia, J.E., 1992. Estimating incident and reflected wave field using an arbitrary number of wave gauges. In: Proceedings of International Conference on Coastal Engineering. vol. I, 777–789.